RESEARCH ARTICLE

WILEY

Multicomponent topology optimization of functionally graded lattice structures with bulk solid interfaces

Bing Yi[1] | Kazuhiro Saitou[2]

[1]School of Traffic and Transportation Engineering, Central South University, Changsha, China

[2]Department of Mechanical Engineering, University of Michigan, Ann Arbor, Michigan, USA

Correspondence
Bing Yi, School of Traffic and Transportation Engineering, Central South University, Changsha, China.
Email: bingyi@csu.edu.cn

Abstract

This article presents a topology optimization method for structures consisting of multiple lattice components under a certain size, which can be manufactured with an additive manufacturing machine with a size limit and assembled via conventional joining processes, such as welding, gluing, riveting, and bolting. The proposed method can simultaneously optimize overall structural topology, partitioning to multiple components and functionally graded lattices within each component. The functionally graded lattice infill with guaranteed connectivity is realized by applying the Helmholtz PDE filter with a variable radius on the density field in the solid isotropic material with penalization (SIMP) method. The partitioning of an overall structure into multiple components is realized by applying the discrete material optimization (DMO) method, in which each material is interpreted as each component, and the size limit for each component imposed by a chosen additive manufacturing machine. A gradient-free coating filter realizes bulk solid boundaries for each component, which provide continuous mating surfaces between adjacent components to enable the subsequent joining. The structural interfaces between the bulk solid boundaries are extracted and assigned a distinct material property, which model the joints between the adjacent components. Several numeral examples are solved for demonstration.

KEYWORDS

bulk solid interfaces, lattice infill, multicomponent structures, topology optimization

1 | INTRODUCTION

Lattice structures exhibit superior structural properties such as low stiffness-to-weight ratio, robustness for random direction loads, damage resistance against defects, and extreme physical properties such as large energy absorption,[1,2] negative Poisson's ratio,[3,4] large thermal expansion,[5,6] and special acoustic absorption.[7,8] Owing to the recent advancement in additive manufacturing processes, especially those in metals, the fabrication and testing of engineered lattice structures have become much more accessible to researchers. Thompson et al.[9] reviewed recent work on design for additive manufacturing including the design of engineered lattice structures. They pointed out there was still a lack of systematic design method to overcome the complexity of lattice structures whose dimension spans from the micro/meso-scale to macro-scale. In addition to the structural complexity, additively manufactured lattice structures for industrial applications
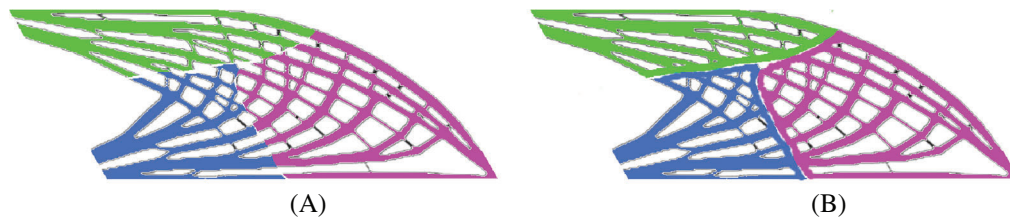
FIGURE 1 Two types of interface between lattice components: (A) no bulk solid interface (extremely difficult to join) and (B) bulk solid interface (straightforward to join)

would be subject to the physical and economical constraints imposed by additive manufacturing processes. In particular, the maximum printing size for the available additive manufacturing machines (within budget) can be a significant design constraint. While a large scale additive manufacturing machines (e.g., Reference 10) are being developed, it still suffers from low precision, large distortion, and limitation of compatible materials.

A remedy to the size limitation of additive manufacturing is to print multiple smaller components and then assemble them to a large structure, as commonly done in the conventional manufacturing processes. For engineered lattice structures, the idea is analogous to the multidomain crystal structures that were proposed to enhance the mechanical behavior of engineered crystalline materials.[11] The difference, however, is that the lattice components produced separately by additive manufacturing would have to be assembled subsequently using joining processes such as welding, gluing, riveting, and bolting. Since it would be practically infeasible to reliably and economically join *each* of numerous meso-scale geometric features that make up individual lattices (Figure 1(A)), each lattice component should have bulk solid boundary that provide adjacent components with continuous mating surfaces that enable the subsequent joining (Figure 1(B)).

This article presents a topology optimization method for structures consisting of multiple lattice components, which can be manufactured via additive manufacturing and then assembled via conventional joining processes. Each component has functionally graded lattice infill surrounded by a bulk solid boundary, which greatly facilitates its assembly via the conventional joining processes such as welding, gluing, riveting, and bolting. The proposed method can simultaneously optimize overall structural topology, its partitioning to multiple components, and functionally graded lattice infill within each component. Structural compliance is considered as the objective function, and constraints are imposed on the volume of the entire structure, the size of each component, and the amount of the bulk solid boundaries around and the joints between components. Based on our previous work on the topology optimization of the assemblies of additively manufactured solid components[12] and functionally graded monolithic lattice structures[13] (which, in turn, is based on Reference 14), the novelty of the proposed method beyond these works is three-fold: it realizes 1) multiple functionally graded lattice components with guaranteed connectivity of lattices therein, 2) the bulk solid boundaries for each component, which provide continuous mating surfaces between adjacent components, and 3) the structural interfaces between the bulk solid boundaries with a distinct material property, which model the joints (e.g., weld, glue, rivets, and bolts) between the adjacent components.

The article is organized as follows. Section 2 discusses related work and Section 3 describes the mathematical formulation of the optimization problem. Several numerical examples are presented in Section 4. Finally, Section 5 concludes the article with discussion of possible future work. The sensitivities of the objective function and constraints are outlined in Appendix A.

2 | RELATED WORK

2.1 | Optimal design of multicomponent structures

Most structural products are made as assemblies of components with simpler geometry. Despite the sacrifice in structural performances due to the introduction of joints, multicomponent assemblies are preferred, or often the only choices in industry, primarily due to economical reasons—the manufacturing and assembly of multiple components with simpler geometry is often far less costly than of a monolithic structure with complex geometry. *Assembly synthesis* is a process of partitioning a structure into multiple components, each with simpler geometry, to enhance the ease of manufacturing.

By viewing the problem as the optimal balance between structural performance and manufacturing cost, computational optimal assembly synthesis for structural products were attempted in References 15,16 for stamped sheet metal structures and in Reference 17 for extruded space frame structures. In the field of computer graphics, there also is recent work addressing the partitioning of product geometry into smaller components, so each can fit within the maximum printer size for additive manufacturing.[18-20] However, these work only deal with manufacturability-driven partitioning of prescribed fixed geometries without considering the optimization of the overall product geometries.

Early work on topology optimization of multicomponent structures, on the other hand, was the optimization of the overall product geometry with prescribed fixed partitioning, where each component is optimized within the prescribed design domain, and joints are optimized within the overlaps among these domains.[21-25] In these work, therefore, an optimized structure must be an assembly of prescribed number of components with prescribed adjacency. Considering that joints are usually structurally inferior to components and therefore should be introduced only if justifiable by performance-cost balance, this formulation can only explore very small subset of all possible multicomponent structures.

Multicomponent topology optimization (MTO) was motivated by the need of automatically generating optimal structures made as assemblies of multiple ready-to-manufacture components, each of which conforms geometric constraints imposed by a chosen manufacturing process, such as component sizes, undercuts, and uniform wall thickness. Lyu and Saitou,[26] Yildiz et al.,[27] and Guirguis et al.[28] formulated MTO as discrete optimization problems for (2D approximations of) stamped sheet metal assemblies and solved them by genetic algorithms. However, it is extremely time consuming and hence can only solve simple "toy" problems. Zhou and Saitou[29] proposed a continuous relaxation of MTO for 2D stamped sheet metal assemblies, which enabled the use of efficient gradient-based optimization algorithms. Zhou et al.[30] extended the formulation to composite structures, which is capable of simultaneously optimizing the overall topology, component partitioning, and tailored material orientation for each component. By considering the size constraint of the additive manufacture machines, Zhou et al.[12] presented a MTO formulation for additive manufacturing with a build volume constraint. Despite its promise, MTO is still at an infancy and yet to become robust enough for industry applications. These researches, in particular, have only considered bulk solid structures or 2D approximation of thin-wall structures.

Recently, Francesco et al.[31] presented a method to optimize the distribution of the lattice infill in multiple domains by using two-step method consisting of domain boundary optimization followed by infill lattice optimization. Gao et al.[32] also proposed a multiscale topology optimization method for the design of porous composites composed of the multidomain material microstructures. In these work, however, multiple domains are defined within a single structure that is assumed to be produced as one piece, with no considerations of manufacturing constraints. To the best of the author's knowledge, there is no previous research work considering the topology optimization of structural assemblies consisting of multiple lattice components driven by the manufacturability of each component and the assembleability of multiple components, such as the ones addressed in this article.

2.2 | Interface modeling in multidomain structures

While a model of structural interfaces between adjacent components (i.e., joints) were included in the discrete formulation of MTO,[26-28] it was based on the discrete representations of component boundaries, which required the use of inefficient non-gradient optimization algorithms.

A related problem of modeling interfaces between distinct materials has been discussed in the area of multimaterial topology optimization. Most work utilizes level set based topology optimization, since it has an advantage of representing explicit boundaries between material phases at each iteration of optimization. Vermaak et al.[33] proposed a framework for the modeling of material interface properties in multiphase elastic and thermoelastic structures, which can model the material interfaces with monotonic and non-monotonic property variations. Faure et al.[34] extended this method for the modeling of smooth and graded transitions for micro-structures and investigated the influence of graded interfaces in multimaterial topology optimization. Liu et al.[35] presented monolothic topology optimization of structures that embed prescribed components with fixed geometry, with the interface model between the embedding structure and embedded component.

Little work has been published on material interface modeling based on the solid isotropic material with penalization (SIMP) method, where the "gray" zones that always exist between two material phases pose challenges in modeling material interfaces. Francesco et al.[31] proposed the framework for the modeling of solid internal interface for lattice infill structures by using the artificial threshold for the density field. Chu et al.[36] proposed the graded interface modeling of multimaterial topology optimization,[36] which employs the coating filter proposed by Clausen et al.[37] The filter, however,

requires computing the maximum of the norm of the gradient vector of the density field, which poses numerical challenges both in efficiency and accuracy. To overcome this challenge, Yoon et al.[38] proposed simple two-step filtering for the topology optimization of coated structures without the need of density gradient.

3 | DESIGN MODEL

3.1 | Overview

Three fields are defined to represent the design model for a structural assembly of functionally graded lattice components with continuous component interface: material density ρ, radius r_l for local density averaging, and component membership vector $\mathbf{m} = (m^{(1)}, m^{(2)}, \dots, m^{(K)})$, where K is the prescribed maximum allowable number of components. Figure 2 illustrates an instance where $K = 3$. The overall structure with functionally graded lattice is represented as filtered density field ρ by variable-radius Helmholtz PDE filter with radius r_l.[13] The multiple components within the overall structure are represented as a fractional membership $m^{(k)}$ to each component k, where $k = 1, 2, \dots, K$ in a similar manner DMO represents multiple material orientations[12] (Figure 2(A)). The bulk solid boundaries for each component are obtained by applying the coating filters in Reference 38 for each element $m^{(k)}$ of the component membership vector field $\mathbf{m}$ (Figure 2(B)). With the carefully controlled filter radii, the joints between the mating boundaries are extracted as the overlap region of the coatings of two adjacent components. Finally, the design model is constructed by compiling the overall lattice structure, component membership, and the bulk solid boundaries and joints (Figure 2(C)).

3.2 | Functionally graded lattice structures

Let $\phi : D \rightarrow [-1, 1]$ be the (unregularized) design variable, where D is a fixed design domain. To avoid checkerboard patterns and achieve mesh-independent results, design variable ϕ is regularized by the Helmholtz PDE filter:[39]

$$-r_\rho^2 \nabla^2 \overline{\phi} + \overline{\phi} = \phi, \tag{1}$$

where r_ρ is the filter radius for smoothing, and $\overline{\phi}$ is the smoothed design variable. Then, density field $\rho : D \rightarrow [0, 1]$ is obtained by using a smoothed Heaviside function $H_s : \mathbb{R} \rightarrow [0, 1]$ for the regularized design variable as follows:

$$\rho = H_s(\overline{\phi}). \tag{2}$$

Filtered density　　Membership 1　　Membership 2　　Membership 3

(A)

Boundaries and joints　　Boundary 1　　Boundary 2　　Boundary 3

(B)

Lattice structure　　Component 1　　Component 2　　Component 3
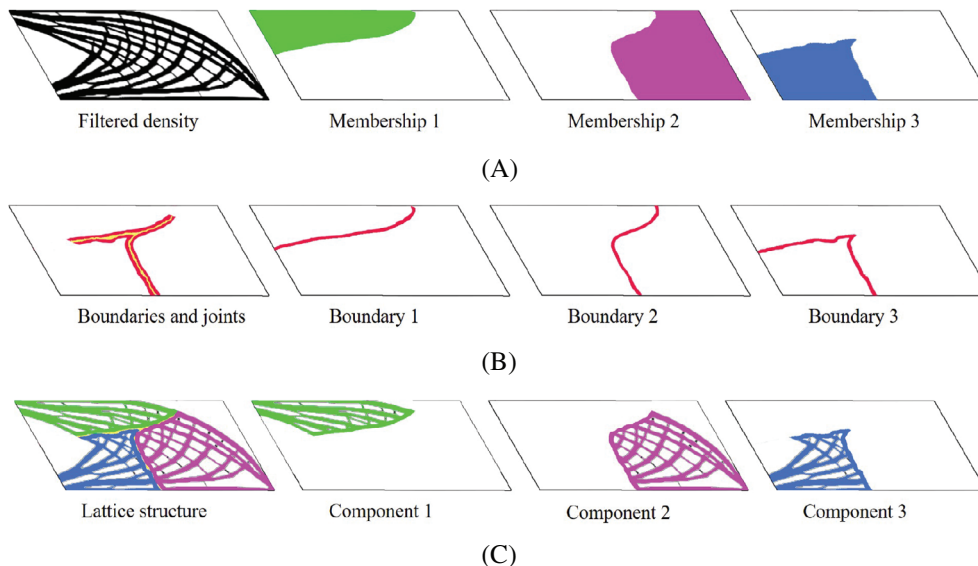
(C)

FIGURE 2 overview of the design model: (A) design fields, (B) bulk solid boundaries and joints, and (C) the compiled design model

Functionally graded lattices can be realized by imposing an upper bound on density values ρ averaged over a small neighborhood, and letting the upper bound vary at each design point in D.[13] To compute locally regularized, "average" material density field ρ_l, the Helmholtz PDE filter is adopted again:

$$-r_l^2 \nabla^2 \rho_l + \rho_l = \rho, \tag{3}$$

where r_l is the (variable) filter radius for averaging density around a design point. If the lower bound of r_l is set to be larger than the (constant) filter radius r_ρ for the regularization of the density field, the functionally graded lattices can be obtained by imposing the upper bound P_{max} on locally averaged density ρ_l:

$$\rho_l \leq P_{max}. \tag{4}$$

Equation (4) should be defined for each design point, which may cause numerical difficulty during optimization. Hence, it can be rewritten equivalently as:

$$\max_{x \in D}(\rho_l) \leq P_{max} \tag{5}$$

and further approximately as:

$$\left(\int_D \rho_l^p \, dx \right)^{\frac{1}{p}} \leq P_{max}, \tag{6}$$

which is differentiable with respect to ϕ and ρ_l. As power p of the p-norm approximation goes to infinity, Equation (6) becomes equivalent to Equation (4). In this article, $p = 10$ is used since larger values will increase numerical instability during optimization.

3.3 | Multicomponent partitioning

Similar to the density field, component membership is represented by a (unregularized) design variable $\mu^{(k)} : D \to [0, 1]$. To achieve mesh independency of component boundary, deign variable $\mu^{(k)}$ is regularized by the Helmholtz PDE filter:

$$-r_\mu^2 \nabla^2 \overline{\mu}^{(k)} + \overline{\mu}^{(k)} = \mu^{(k)}, \tag{7}$$

where r_μ is the filter radius for the controlling of the maximum width of the bulk solid boundaries and the joints, as discussed in the following section.

To encourage that each design point belongs to a unique component at the convergence of the optimization, the DMO projection[40] is applied to the smoothed membership field $\overline{\mu}^{(k)}$ as follows:

$$m^{(k)} = \left\{ \overline{\mu}^{(k)} \right\}^{p_m} \prod_{i=1, i \neq k}^{K} \left[1 - \left\{ \overline{\mu}^{(i)} \right\}^{P_m} \right], \tag{8}$$

where p_m is the penalization parameter to drive each membership vector converge to 0 or 1. As can be seen in Equation (8), an increase in one component membership always leads to a decrease in all the other component memberships. With the DMO projection, the membership vector at a design point will converge to a sparse vector with at most one element being 1 and all the other element being 0, which represents the partition of design domain D to *up to K* components.

3.4 | Bulk solid component boundaries

Our modeling of bulk solid boundaries for each lattice component is inspired by the gradient-free coating filter for SIMP-based (monolithic) topology optimization.[38] Instead of density field ρ that represents the entire structure,

however, the filter is applied to each element $m^{(k)}$ of the component membership vector field, as illustrated in Figure 3.

First, the Helmholtz PDE filter with filter radius r_m, which controls the thickness of the bulk solid boundary, is applied on each element $m^{(k)}$ of component membership vector field:

$$-r_m^2 \nabla^2 \overline{m}^{(k)} + \overline{m}^{(k)} = m^{(k)}, \tag{9}$$

where r_m controls the thickness of the bulk solid boundary, and hence should be $r_m < r_\mu$. Then, a smoothed Heaviside function is applied to the filtered component membership $\overline{m}^{(k)}$ to obtain the field with "crisp" edges:

$$\omega^{(k)} = H_r(\overline{m}^{(k)}) \tag{10}$$

and finally, the membership for bulk solid boundary can be obtained as:

$$b^{(k)} = \{1 - m^{(k)}\} \, \omega^{(k)}. \tag{11}$$

It should be noted that due to its construction, $b^{(k)}$ is bounded between 0 and 1, and therefore will effectively avoid the need of normalization, which is subject to numerical errors for the gradient-based coating filter in Reference 37.

3.5 | Joints

We consider joints as to model the outcome of joining processes such as welding, gluing, screwing, and riveting, which mechanically connects the bulk solid boundaries of two adjacent components. A separate modeling is needed for the joint regions, since they have different, often inferior, material property from the component material. This can be accomplished by extracting a narrow overlap between the two adjacent bulk solid boundaries.

Figure 4 illustrates a (2D) close-up view of the interface between two adjacent components k and l at the optimization convergence, overlaid with the corresponding values of smoothed component membership $m^{(k)}$ and $m^{(l)}$ in Equation (8). The regions with rapid decrease in $m^{(k)}$ and $m^{(l)}$, colored with the gradation from yellow to green for each of component, represent the bulk solid boundaries as defined by $b^{(k)}$ and $b^{(l)}$ in Equation (11). The characteristics of the Helmholtz PDE filter[39] suggests this region approximately has width $r_m/2\sqrt{3}$ for each component, where r_m is the filter radius in Equation (9). Similarly, the entire interface region consisting the (potentially) overlapping regions of bulk solid boundaries (and any space in-between), approximately has width $r_\mu/2\sqrt{3}$, where r_μ is the filter radius in Equation (7). Under an appropriate setting of these filter radii satisfying $r_\mu/2 < r_m < r_\mu$, there will be a small overlap between two regions of bulk solid boundaries $b^{(k)}$ and $b^{(l)}$, which can be extracted as a joint. Since this overlapping region would have near zero component membership values, joint membership J_{kl} is obtained by scaling up $b^{(k)}$ and $b^{(l)}$:

$$J^{(kl)} = \left\{m_0 + b^{(k)}(1 - m_0)\right\} \left\{m_0 + b^{(l)}(1 - m_0)\right\}, \tag{12}$$

where $l \neq k$ and m_0 is a small positive number, that defines the lower bound for the scaling. For notational convenience, $J^{(kl)}$ is defined as 0 for $l = k$.
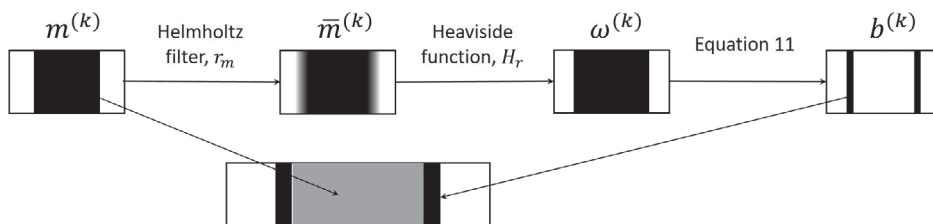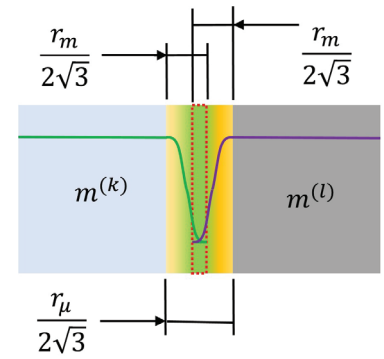

FIGURE 3 Simple two-step filtering approach for modeling bulk solid component boundaries

3.6 | Interpolation functions

For simplicity as an initial attempt, the infill lattices, bulk solid boundaries, and joints are all assumed to be isotropic in this article. Similar to conventional SIMP method, the Young's modulus of lattice infill for component k, excluding the bulk solid boundaries and joints, is given as:

$$E_\rho^{(k)} = E \left\{ \rho^{p_\rho} m^{(k)} - b^{(k)} - \sum_{l=1}^{k} J^{(kl)} \right\}, \tag{13}$$

where E is the Young's modulus of the component material and p_ρ is the SIMP penalization parameter. The sum for J^{kl} is taken over $l = 1, 2, \ldots, k$ instead of $l = 1, 2, \ldots, K$ to avoid "double counting" of the joint region when the contribution of all K components are summed together. The bulk solid boundaries of component k, excluding the overlapping regions which are considered as joints, are also made from the component material:

$$E_b^{(k)} = E \left\{ b^{(k)} - \sum_{l=1}^{K} J^{(kl)} \right\}. \tag{14}$$

In this case, the sum for J^{kl} is taken over $l = 1, 2, \ldots, K$ since the joints are defined in the *overlapping* region of $b^{(k)}$ and $b^{(l)}$. The Young's modulus for the joint between components k and $l = 1, 2, \ldots, K$ is given as:

$$E_J^{(k)} = \eta E \sum_{l=1}^{k} J^{(kl)}, \tag{15}$$

where η is the ratio of the Young's modulus of the joint material to the one for the structural material. Similar to Equation (13), the sum is taken over $l = 1, 2, \ldots, k$. Finally, the Young's modulus for each point in the design domain can be defined as:

$$E_t = \sum_{k=1}^{K} \left\{ E_\rho^{(k)} + E_b^{(k)} g(\rho_l) + E_J^{(k)} \right\}, \tag{16}$$

where $g(\rho_l)$ is an interpolation function to enable a smooth transition from infill lattices to bulk solid boundaries. Using the fact that $\sum_{k=1}^{K} \sum_{l=1}^{K} = 2 \sum_{k=1}^{K} \sum_{l=1}^{k}$, Equation (16) can be rewritten as:

$$E_t = E \sum_{k=1}^{K} \left[\rho^{p_\rho} m^{(k)} - \{1 - g(\rho_l)\} b^{(k)} - \{1 + 2g(\rho_l) - \eta\} \sum_{l=1}^{k} J^{(kl)} \right]. \tag{17}$$

3.7 | Optimization model

The optimization model is formulated as compliance minimization subject to constraints on structural volume, component size, maximum allowable local average density, component interface cost, and maximum allowable number of

component:

$$
\begin{aligned}
\underset{\phi,\mu,r_l}{\text{minimize}} \quad & \mathbf{U}^{\mathrm{T}}\mathbf{KU} \\
\text{subject to:} \quad & \mathbf{KU} = \mathbf{F} \\
& \int_D \sum_{k=1}^{K} \rho m^{(k)} dx \leq V_{max} \\
& \left(\int_D \rho_l^p dx \right)^{\frac{1}{p}} \leq P_{max} \\
& R^{(k)} \leq R_{max}; \qquad k = 1, 2, \ldots, K \\
& C \leq C_{max} \\
& \phi \in [-1, 1]^D \\
& \mu^{(k)} \in [0, 1]^D; \qquad k = 1, 2, \ldots, K \\
& r_l \in [r_\rho, 5r_\rho]^D,
\end{aligned}
\tag{18}
$$

where $\mathbf{K}$, $\mathbf{U}$, and $\mathbf{F}$ are the stiffness matrix, the displacement vector, and the force vectors of the finite element mesh of domain D, respectively; V_{max}, R_{max}, and C_{max} are the maximum allowable volume of the entire structure, the maximum radius of the printable sphere for the additive manufacturing machine, and the maximum allowable amount for the bulk solid boundaries and joints within the structure, respectively.

Instead of rectangular (prismatic) bounding boxes adopted in References 12,29, the components sizes are approximated by their bounding spheres for the sake of computational simplicity. The radius of the bounding sphere of component k is given as:

$$
R^{(k)} = \max_{x \in D} \| \rho m^{(k)} \{ x - x_c^{(k)} \} \| \approx \left[\int_D \rho m^{(k)} \{ x - x_c^{(k)} \}^p dx \right]^{\frac{1}{p}},
\tag{19}
$$

where $x_c^{(k)}$ is the centroid of component k:

$$
x_c^{(k)} = \frac{\int_D \rho m^{(k)} x dx}{\int_D \rho m^{(k)} dx}.
\tag{20}
$$

The total amount of the bulk solid boundaries and joints within the structure is approximated as:

$$
C = \sum_{k=1}^{K} \left[\int_D g(\rho_l) \left\{ m^{(k)} - \sum_{l=1}^{k} J^{(kl)} \right\} dx \right].
\tag{21}
$$

This amount needs to be constrained by the maximum allowable amount in Equation (18), since otherwise the optimizer tends to exploit the solid bulk boundaries to minimize the compliance objective and place them everywhere in the structure.

For the examples in the next section, the optimization model in Equation (18) is implemented with MATLAB and COMSOL is used for solving FEM and optimization. The method of moving asymptotes (MMA)[41] is adopted as the optimization algorithm. The derivations of the sensitivities of the objective function and constraints are outlined in Appendix A.

4 | EXAMPLES

This section presents two simple examples on a cantilever beam and an MBB and an industry example on a railcar body profile for high-speed trains. In all examples, the design domains are discretized with identical square four-node elements with size $r_e = 0.02$, and filter radius r_ρ in Equation (1) is set as r_e. The design variables are initialized as $\phi = 0$ and $\mu^{(k)} = 0.5$
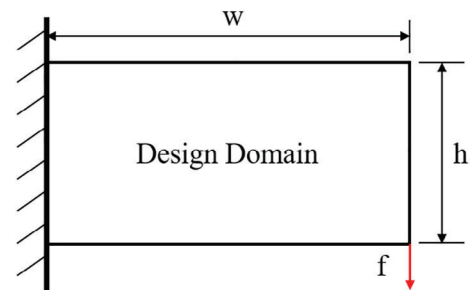
TABLE 1 Common parameter values in the examples

Symbol	Definition	Value
p_ρ	SIMP penalty	3
p_m	Membership penalty	6
p	p-norm power	10
E	Young's modulus	1
υ	Poisson's ratio	0.3
P_{max}	Max. local density	0.6

TABLE 2 Other input parameters for the examples

Symbol	Definition
K	Maximum allowable number of components
E_{joint}	Young's modulus of the joint material ($= \eta E$ in Equation 15)
r_ρ	Filter radius for density (Equation 1)
r_m	Filter radius for membership vector (Equation 9)
V_{max}	Max. volume of the entire structure (Equation 18)
R_{max}	Max. radius of the printable sphere (Equation 18)
C_{max}	Max. amount for bulk solid boundaries and joints (Equation 18)

FIGURE 5 Design domain and boundary conditions for the cantilever problem

uniformly in the design domain. Tables 1 summarizes the parameter values common in the examples. As a recap, Table 2 lists the other input parameters that can take various values in the examples.

4.1 | Cantilever beam

The design domain is a rectangle area of unit thickness with width $w = 2$ and height $h = 1$, and a concentrated load $f = 1$ is applied at the lower right corner of the rectangle, as shown in Figure 5.

The iteration snapshots are shown in Figure 6 for the case with $K = 2$, $E_{joint} = 0.5$, $r_\mu = 3r_e$, $r_m = 1.75r_e$, $R_{max} = 0.55$, and $C_{max} = 0.12$. In each of the subfigure, the first row shows the density and membership fields for each component, the second row shows the joints and bulk solid boundaries for each component, and the third row show the optimized structure and components. Since initially $\phi = 0$ and $\mu^{(k)} = 0.5$ everywhere, density ρ is 0.5, and membership m^k is almost zero due to the DMO projection. As a result, the bulk solid boundary and joints are also almost zero, so are the overall structure and components (Figure 6(A)). As the iteration proceeds, the overall structure and memberships becomes clearer, but the bulk solid boundaries and the joints remains unclear (Figure 6(B)). Then, the memberships quickly become clear between iteration 200 and 400 and so is the solid interface and joints (Figure 6(C)). The overall structures and other quantities appear to reach local optima at iteration 1200 (Figure 6(D)).

Figures 7, 8, and 9 show the results for different joint stiffness with $E_{joint} = 0.25$, 0.5, and 0.75, respectively. For these runs, $K = 2$, $r_\mu = 3r_e$, $r_m = 1.75r_e$, $V_{max} = 0.5$, $R_{max} = 0.55$, and $C_{max} = 0.1$ are used. It can be seen that, the bulk solid boundary (and the joint in between) is straight and short when the Young's modulus of joints is small, and becomes curved

and long as the joint becomes stiffer, taking advantage of the more use of bulk solid boundary, until the upper bound C_{max} is reached. In response to the changes in the boundary, the lattice patterns also change. The von Mises stress of these optimized structures are shown in Figure 10. The maximum stress (shown in red) is observed at the periphery of the structures. The stress is much smaller (shown in blue) in the regions of bulk-solid boundary and joint, since the bulk solid boundaries are much stiffer than the rest of lattice structure. While the joints are less stiff than the lattice structure, the stress there is still smaller than the lattices, since they are "protected" by stiff boundaries.

Figures 11 and 12 show the results for different thickness in bulk solid boundary with $(r_\mu, r_m) = (4r_e, 2.25r_e)$ and $(5r_e, 2.75r_e)$, respectively. For these runs, $K = 2$ and $E_{joint} = 0.5$, $V_{max} = 0.5$, $R_{max} = 0.55$, and $C_{max} = 0.12$ are used. Similar to the results of different joint stiffness, the lattice patterns change in response to the changes in the boundary thickness. Interestingly, both structures show intercomponent gaps formed by bulk solid boundaries without joint material, effectively creating a "lattice" by utilizing bulk solid boundaries. This is because the large thickness of the bulk solid boundaries makes them stiff enough to bear the load by themselves even without forming joints. Indeed, the von Mises stress in the bulk-solid boundaries near the intercomponent gaps is much smaller (blue) than the rest of the structure in

Density field Membership 1 Membership 2

Boundaries and joints Boundary 1 Boundary 2

Overall structure Component 1 Component 2

(A)

Density field Membership 1 Membership 2

Boundaries and joints Boundary 1 Boundary 2

Overall structure Component 1 Component 2

(B)
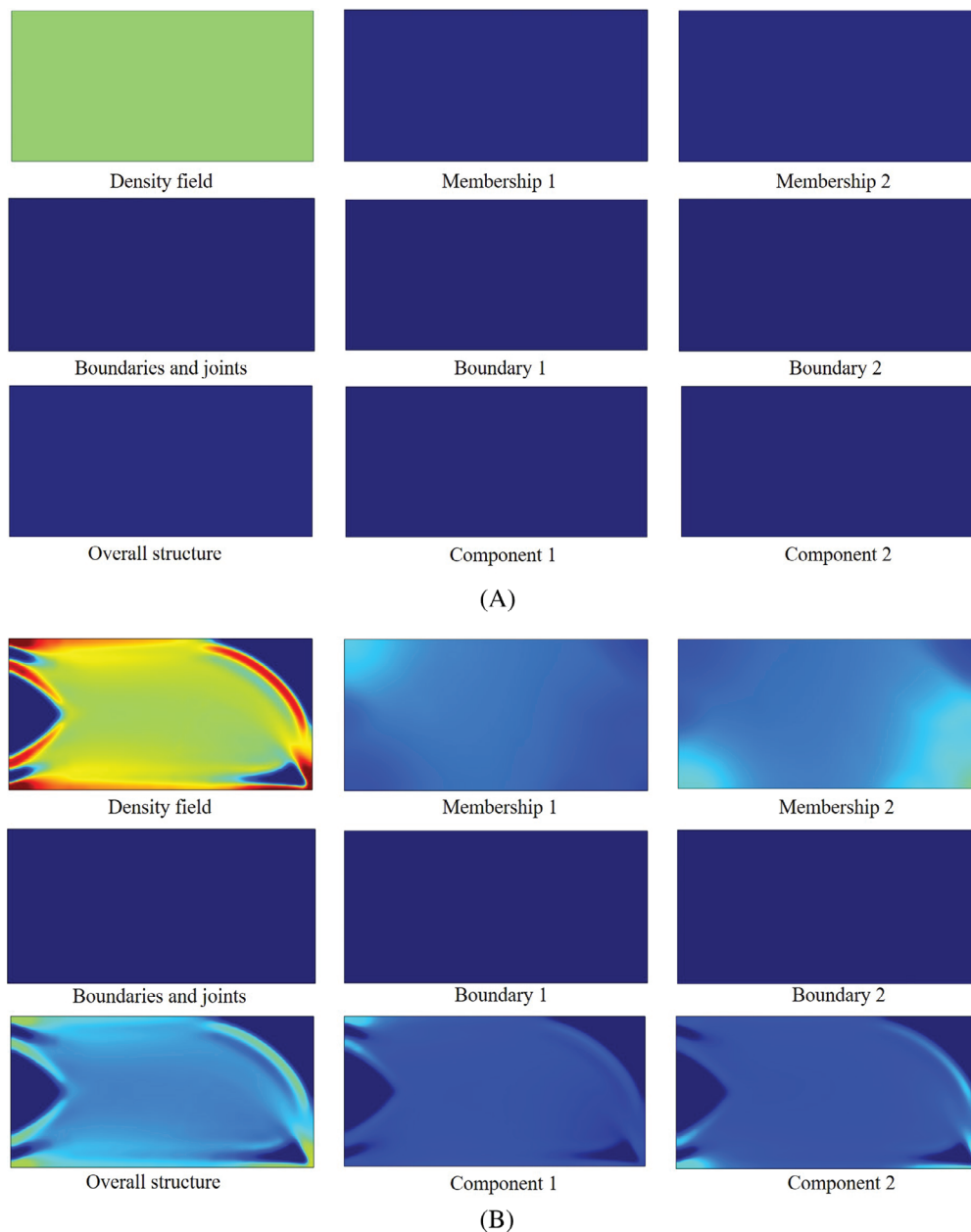
FIGURE 6 (Continued)

FIGURE 6 Iteration snapshots of cantilever beam with $K = 2$, $E_{joint} = 0.5$, $r_\rho = 3r_e$, $r_\mu = 3r_e$, $r_m = 1.75r_e$, $V_{max} = 0.5$, $R_{max} = 0.55$, and $C_{max} = 0.12$: (A) first, (B) 200th, (C) 400th, and (D) 1200th iterations. Its optimized structural compliance is 17.671
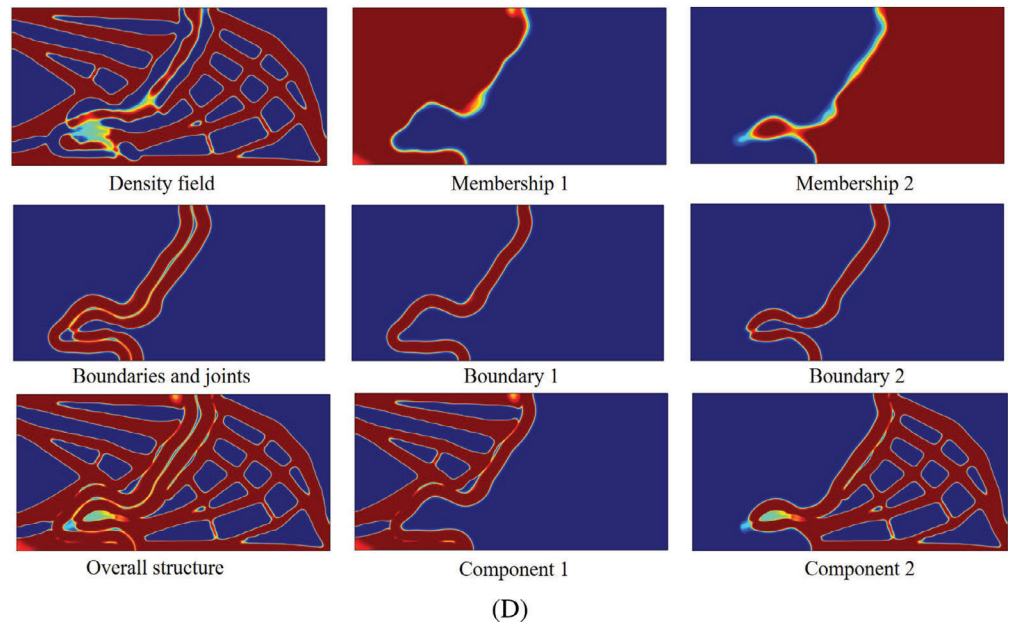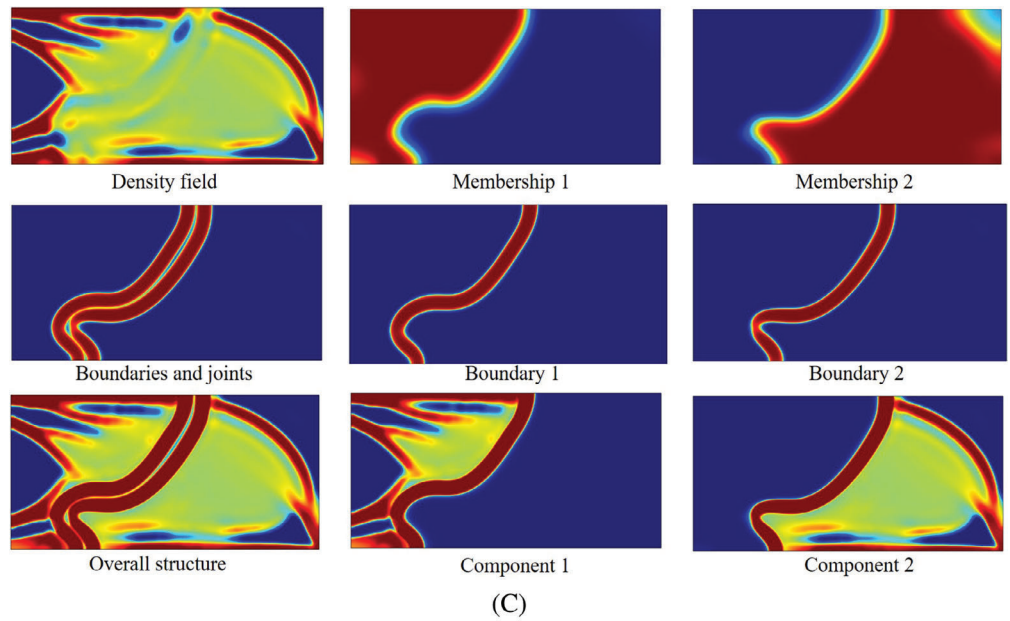

Density field   Membership 1   Membership 2

Boundaries and joints   Boundary 1   Boundary 2

Overall structure   Component 1   Component 2

(C)

Density field   Membership 1   Membership 2

Boundaries and joints   Boundary 1   Boundary 2

Overall structure   Component 1   Component 2

(D)

(A)   (B)   (C)

(D)   (E)   (F)
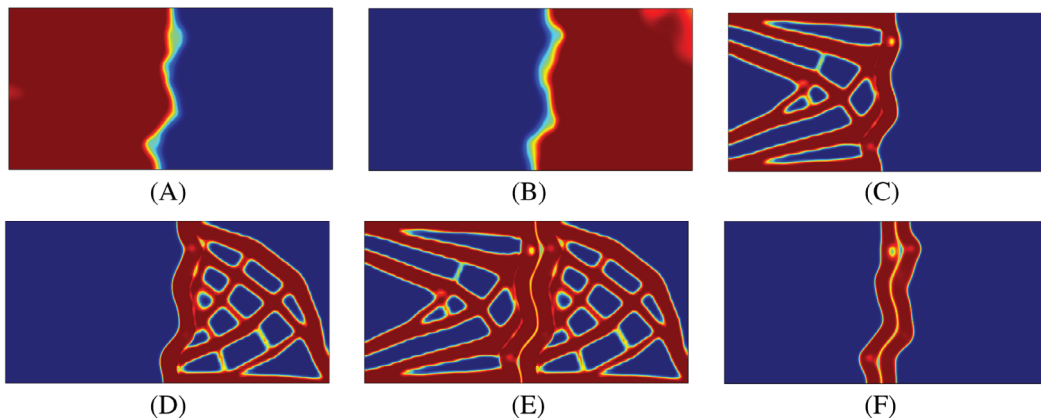
FIGURE 7 Cantilever beam with $K = 2$ and $E_{joint} = 0.25$, $r_\mu = 3r_e$, $r_m = 1.75r_e$, $V_{max} = 0.5$, $R_{max} = 0.55$, and $C_{max} = 0.1$: (A) membership 1, (B) membership 2, (C) component 1, (D) component 2, (E) overall structure, and (F) bulk solid boundary and joint. Its optimized structural compliance is 19.450
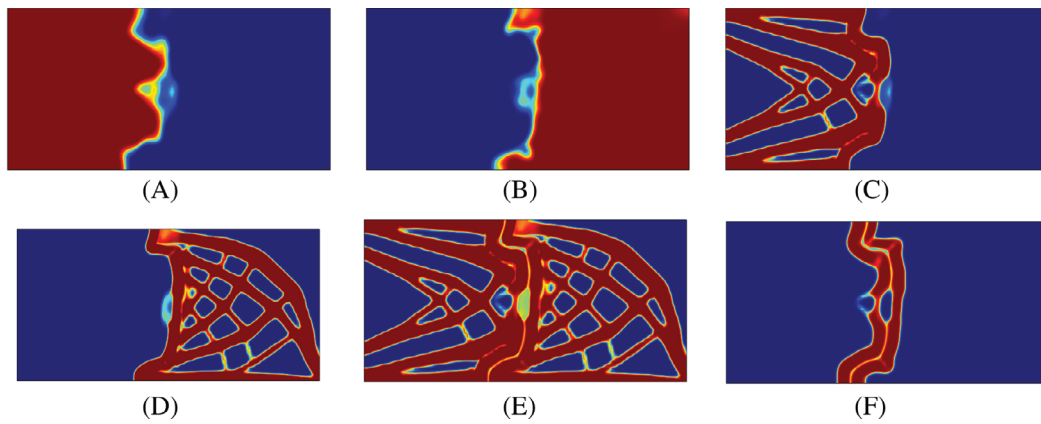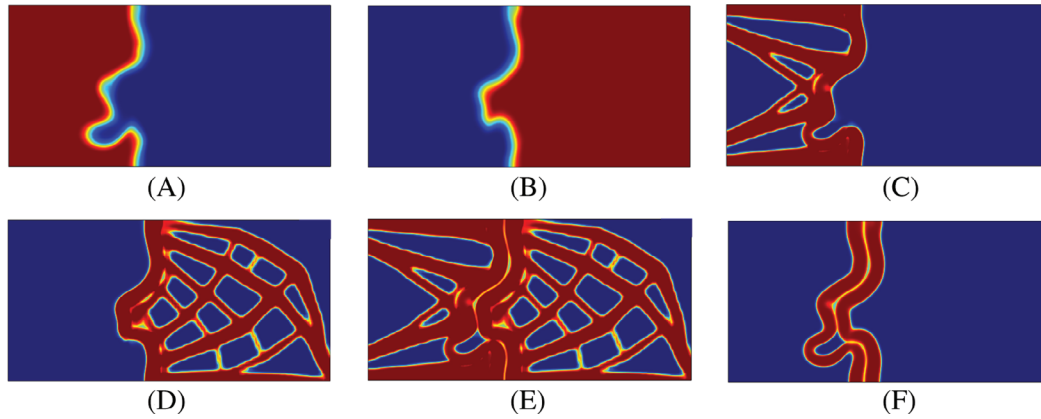
FIGURE 8 Cantilever beam with $K = 2$ and $E_{joint} = 0.5$, $r_\mu = 3r_e$, $r_m = 1.75r_e$, $V_{max} = 0.5$, $R_{max} = 0.55$, and $C_{max} = 0.1$: (A) membership 1, (B) membership 2, (C) component 1, (D) component 2, (E) overall structure, and (F) bulk solid boundary and joint. Its optimized structural compliance is 19.228
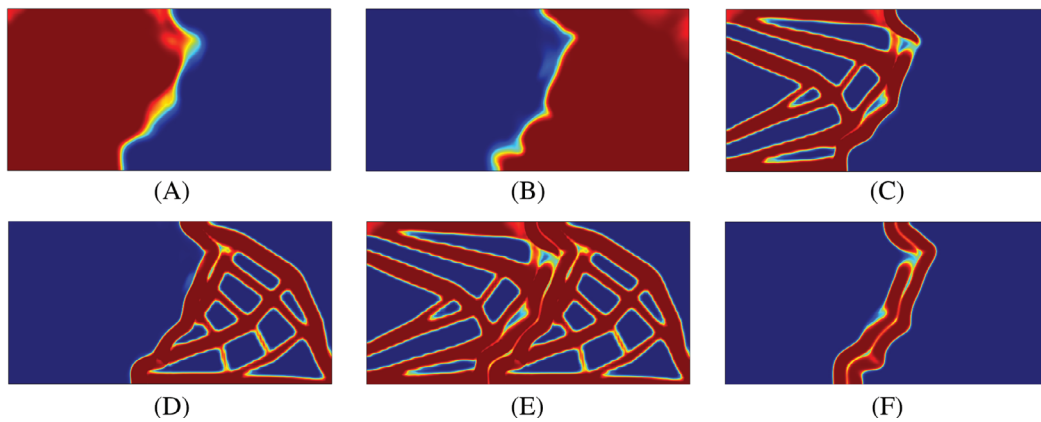
FIGURE 9 Cantilever beam with $K = 2$ and $E_{joint} = 0.75$, $r_\mu = 3r_e$, $r_m = 1.75r_e$, $V_{max} = 0.5$, $R_{max} = 0.55$, and $C_{max} = 0.1$: (A) membership 1, (B) membership 2, (C) component 1, (D) component 2, (E) overall structure, and (F) bulk solid boundary and joint. Its optimized structural compliance is 18.489
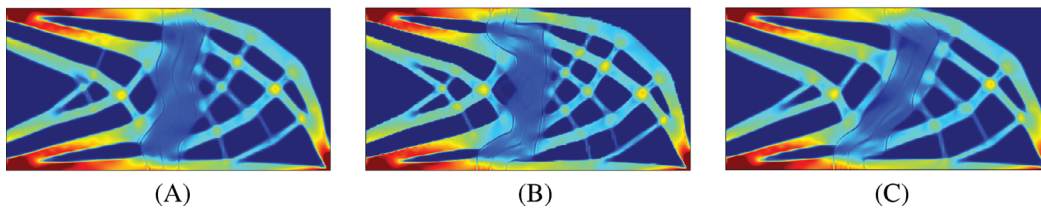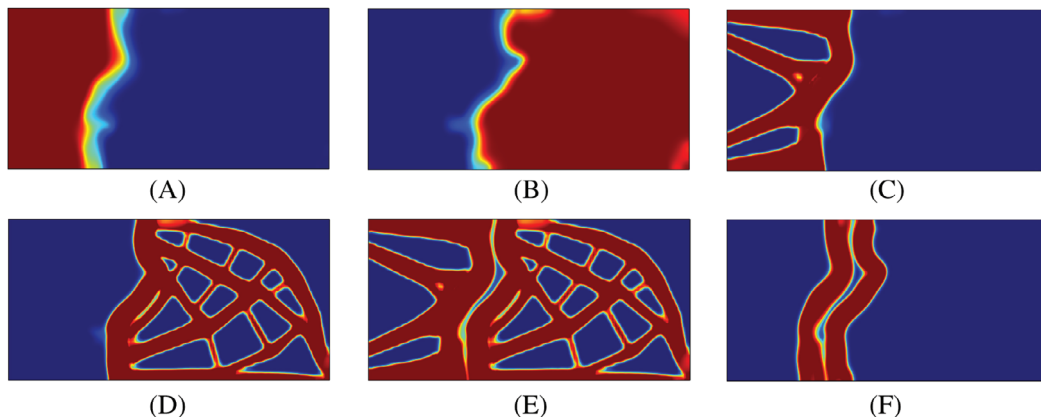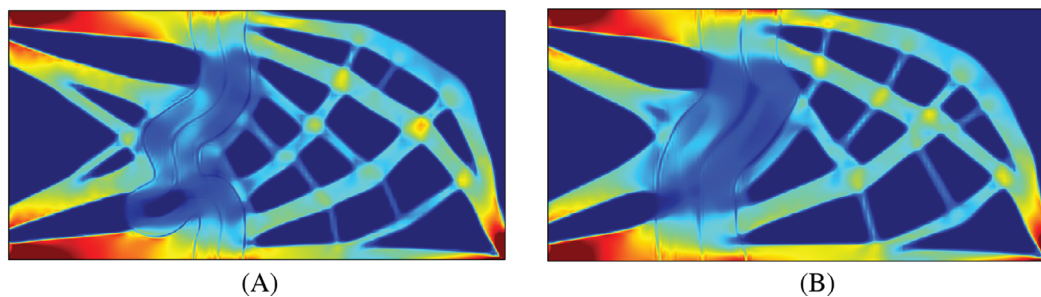

FIGURE 10 Stress of cantilever beam with $K = 2$ and (A) $E_{joint} = 0.25$, (B) $E_{joint} = 0.5$, and (C) $E_{joint} = 0.75$

Figure 13. While mathematically making sense, such intercomponent gaps may not be desirable in industry applications. In that case, the gaps can be easily eliminated by setting a lower value of r_m and/or C_{max}, as shown in Figure 9.

Figures 14 and 15 show the results for different sizes of bounding spheres of each component with $R_{max} = 0.4$ and 0.55, respectively. For these runs, $K = 3$, $E_{joint} = 0.5$, $r_\mu = 4r_e$, and $r_m = 2.25r_e$, $V_{max} = 0.5$, and $C_{max} = 0.12$ are used. For a smaller bounding sphere, the optimized structure is made of three components as shown in Figure 14, whereas the optimizer decides to virtually eliminate one component for a larger bounding sphere (Figure 15). This appears rational, since the joint material is less stiff than the structural material and K only specifies the maximum allowable number of
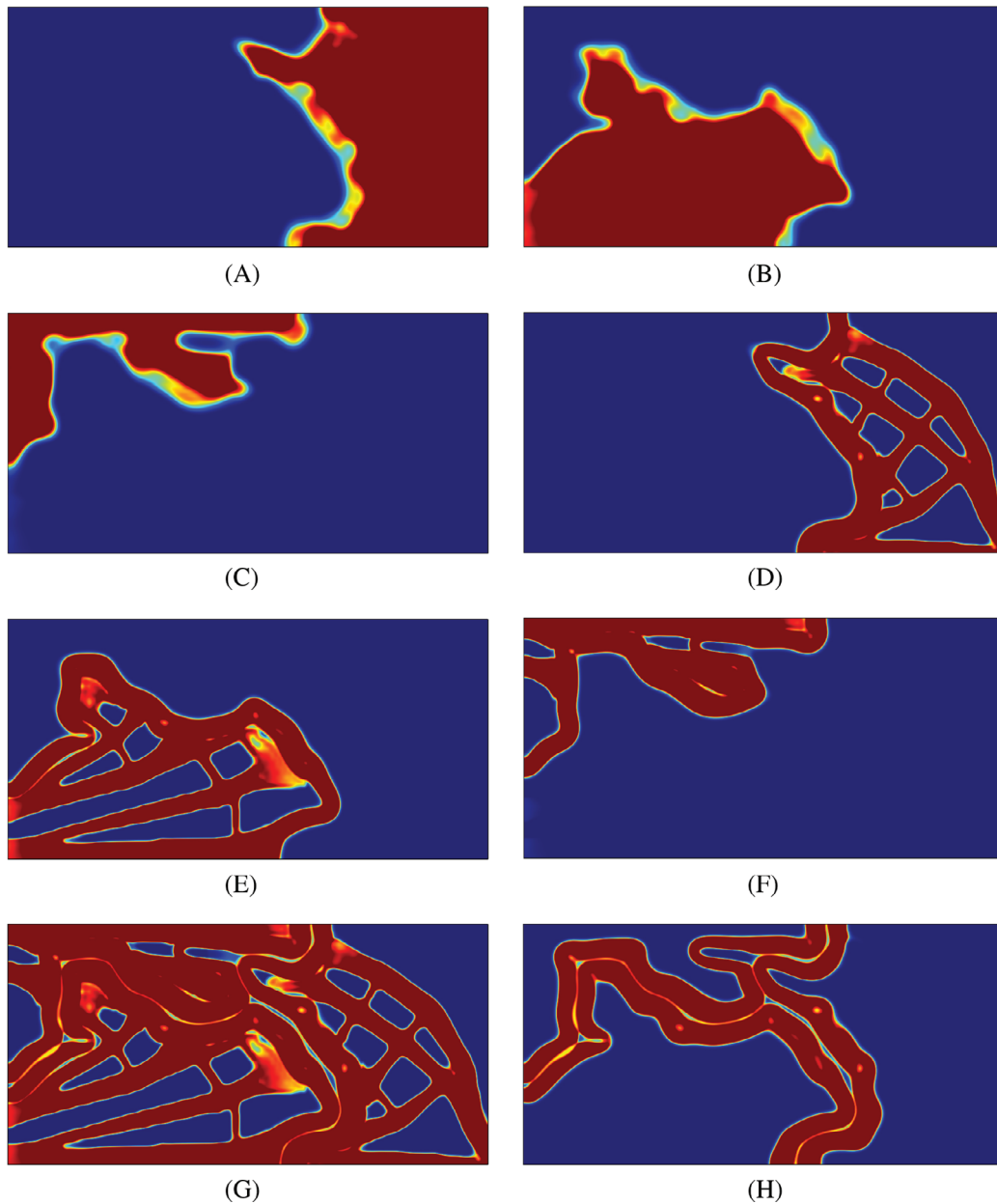
FIGURE 11 Cantilever beam with $K = 2$ and $E_{joint} = 0.5$, $r_\mu = 4r_e$, $r_m = 2.25r_e$, $V_{max} = 0.5$, $R_{max} = 0.55$, and $C_{max} = 0.14$: (A) membership 1, (B) membership 2, (C) component 1, (D) component 2, (E) overall structure, and (F) bulk solid boundary and joint. Its optimized structural compliance is 18.671

FIGURE 12 Cantilever beam with $K = 2$ and $E_{joint} = 0.5$, $r_\mu = 5r_e$, $r_m = 2.75r_e$, $V_{max} = 0.5$, $R_{max} = 0.55$, and $C_{max} = 0.16$: (A) membership 1, (B) membership 2, (C) component 1, (D) component 2, (E) overall structure, and (F) bulk solid boundary and joint. Its optimized structural compliance is 18.317

FIGURE 13 Stress of cantilever beam with $K = 2$ and (A) $r_\mu = 4r_e$, $r_m = 2.25r_e$ and (B) $r_\mu = 5r_e$, $r_m = 2.75r_e$

FIGURE 14 Cantilever beam with $K = 3$, $E_{joint} = 0.5$, $r_\mu = 4r_e$, $r_m = 2.25r_e$, $V_{max} = 0.5$, $R_{max} = 0.40$, and $C_{max} = 0.18$: (A) membership 1, (B) membership 2, (C) membership 3, (D) component 1, (E) component 2, (F) component 3, (G) overall structure, and (H) bulk solid boundary and joint. Its optimized structural compliance is 17.949

components. Both results also show the intercomponent gaps formed by bulk solid boundaries without joint material due to a relatively large value of r_m and C_{max}.

Figures 16 and 17 show the results for different upper limits of the volume of entire structure and the amount of bulk solid boundaries and joints, with $(V_{max}, C_{max}) = (0.5, 0.2)$ and $(0.45, 0.25)$, respectively. For these runs, $K = 3$, $E_{joint} = 0.5$, $r_\mu = 3r_e$, $r_m = 1.75r_e$, and $R_{max} = 0.40$ are used. With large structural volume and small interface amount, the optimal structure consists of more lattice infill (Figure 16), whereas the optimizer utilizes more bulk solid boundaries with smaller structural volume and large interface amount (Figure 17). Despite this difference in the strategy to minimize the compliance objective, the compliance values are comparable: $c = 18.030$ and $c = 18.260$, respectively. Owing to large C_{max}, both structures show the intercomponent gaps, similar to the results in Figures 11 and 12. The von Mises stress of these optimized structures are shown in Figure 18. Similar to the earlier results, the stress is much smaller in the regions of bulk-solid boundary and joint, as well as the intercomponent gaps.
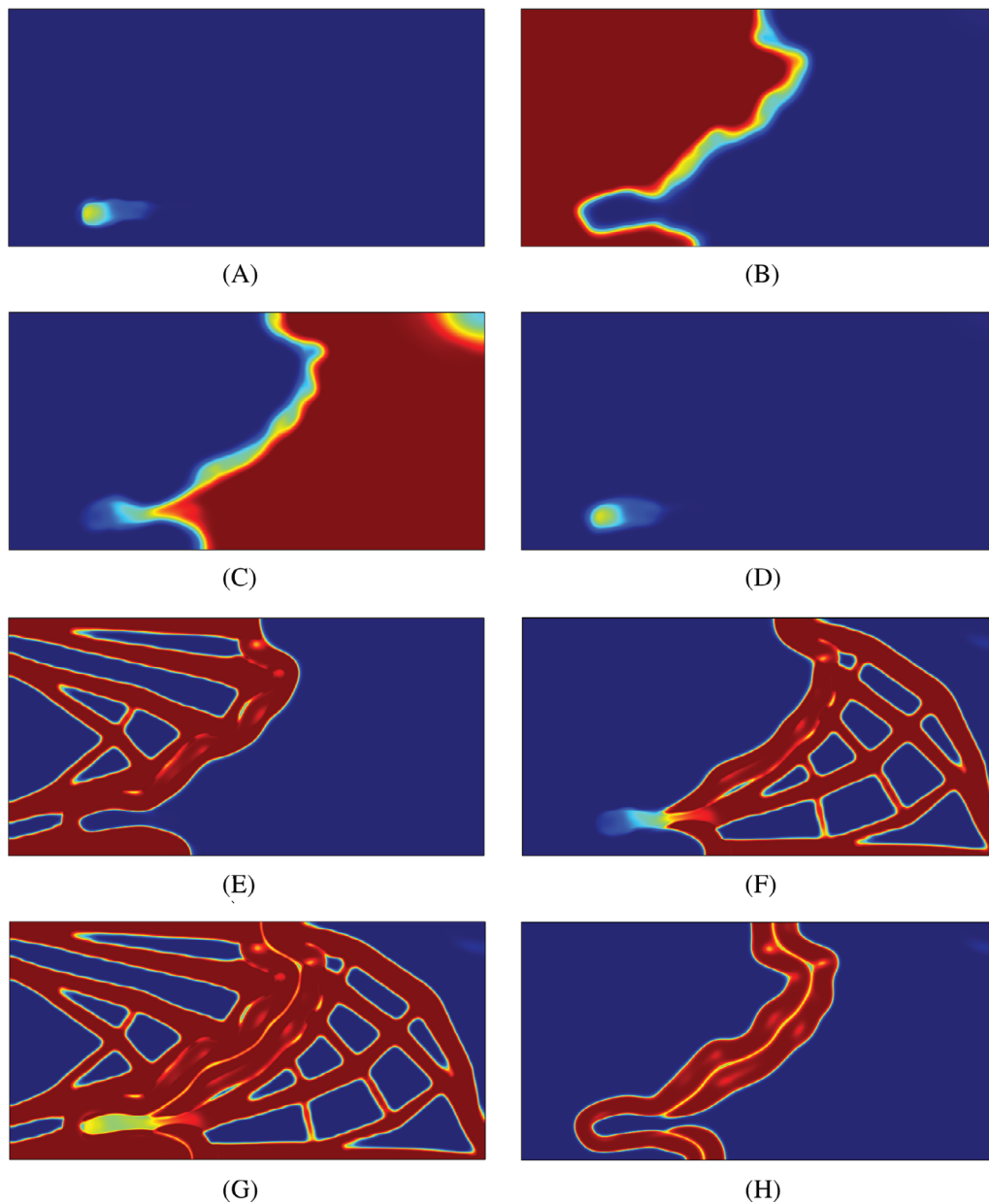
FIGURE 15 Cantilever beam with $K = 3$, $E_{joint} = 0.5$, $r_\mu = 4r_e$, $r_m = 2.25r_e$, $V_{max} = 0.5$, $R_{max} = 0.55$, and $C_{max} = 0.18$: (A) membership 1, (B) membership 2, (C) membership 3, (D) component 1, (E) component 2, (F) component 3, (G) overall structure, and (H) bulk solid boundary and joint. Its optimized structural compliance is 17.542

4.2 | MBB

The design domain is a rectangle area of unit thickness with width $w = 2$ and height $h = 1$ with a symmetry constraint on the left edge, and a concentrated load of $f = 1$ is applied at the upper left corner of the rectangle, as shown in Figure 19.

Figures 20,21, and 22 show the results for different joint stiffness with $E_{joint} = 0.25, 0.5$, and 0.75, respectively. For these runs, $K = 2$, $r_\mu = 3r_e$, $r_m = 1.75r_e$, $V_{max} = 0.5$, $R_{max} = 0.55$, and $C_{max} = 0.1$ are used. Similar to the cantilever example, the bulk solid boundary (and the joint in between) is straight and short with compliant joint and curved and long with stiff joint, with varying lattice patterns. The von Mises stress in Figure 23 shows small stress (shown in blue) in the interface regions, similar to the cantilever example.

Figures 24 and 25 show the results for different thickness in bulk solid boundary with $(r_\mu, r_m) = (4r_e, 2.25r_e)$ and $(5r_e, 2.75r_e)$, respectively. For these runs, $K = 2$ and $E_{joint} = 0.5$, $V_{max} = 0.5$, $R_{max} = 0.55$, and $C_{max} = 0.12$ are used. Similar
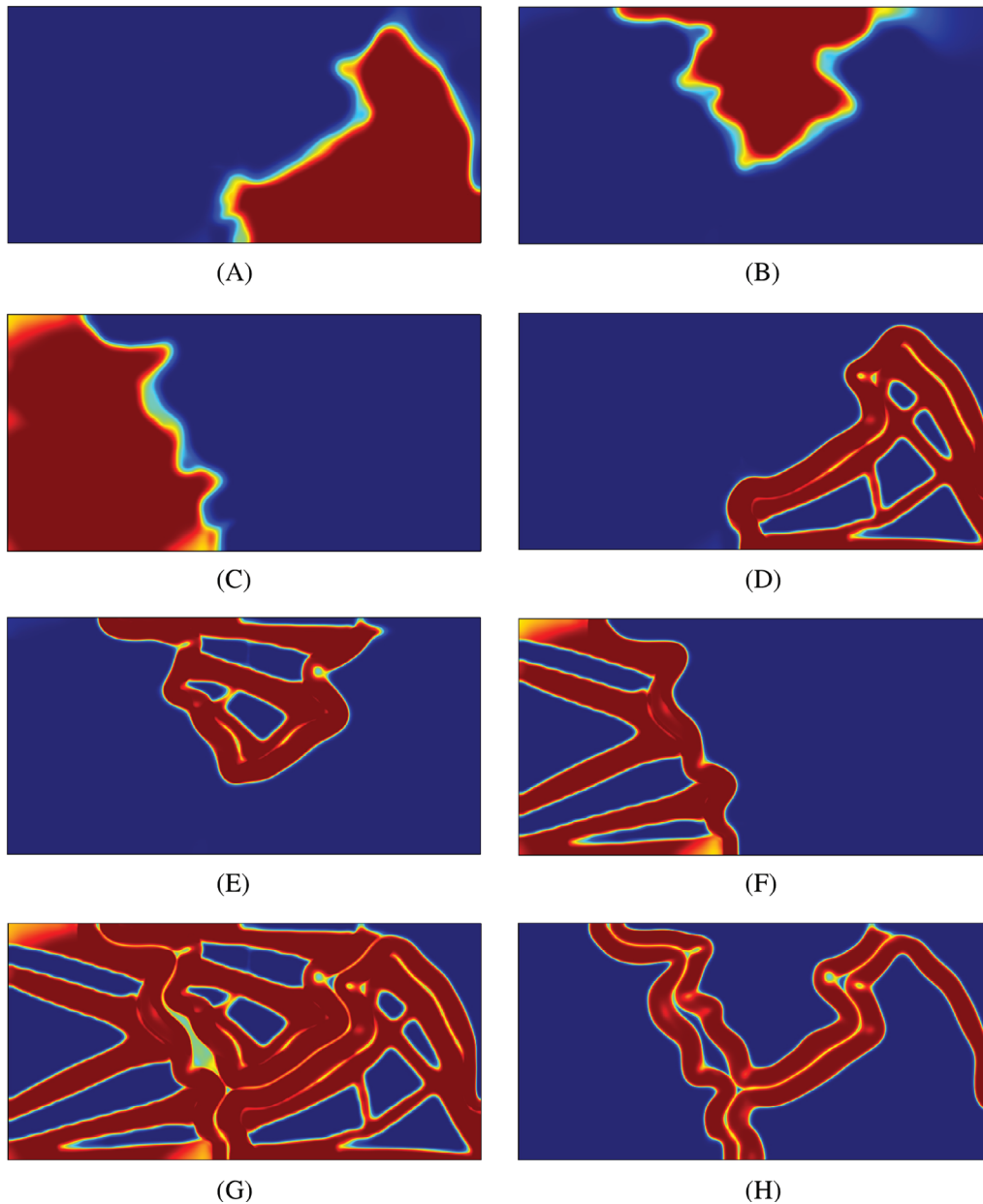
FIGURE 16   Cantilever beam with $K = 3$, $E_{joint} = 0.5$, $r_\mu = 3r_e$, $r_m = 1.75r_e$, $V_{max} = 0.5$, $R_{max} = 0.40$, and $C_{max} = 0.2$: (A) membership 1, (B) membership 2, (C) membership 3, (D) component 1, (E) component 2, (f) component 3, (G) overall structure, and (H) bulk solid boundary and joint. Its optimized structural compliance is 18.260

to the cantilever case, the lattice patterns and the intercomponent gaps change in response to the changes in the boundary thickness. The von Mises stress of these optimized structures in Figure 26 shows low stress in the interface regions including the intercomponent gaps.

Figures 27 and 28 show the results for different sizes of bounding spheres of each component with $R_{max} = 0.4$ and 0.55, respectively. For these runs, $K = 3$, $E_{joint} = 0.5$, $r_\mu = 4r_e$, and $r_m = 2.25r_e$, $V_{max} = 0.5$, and $C_{max} = 0.12$ are used. Similar to the cantilever case, the resulting structure is made of three components for a smaller bounding sphere, and of two components for a larger bounding sphere, and both with the intercomponent gaps due to a relatively large value of r_m and C_{max}.

Figures 29 and 30 show the results for different upper limits of the volume of entire structure and the amount of bulk solid boundaries and joints, with $(V_{max}, C_{max}) = (0.5, 0.25)$, and $(0.45, 0.35)$, respectively. For these runs, $K = 3$, $E_{joint} = 0.5$, $r_\mu = 3r_e$, $r_m = 1.75r_e$, and $R_{max} = 0.40$ are used. Similar to the cantilever case, the optimal structure consists of more lattice
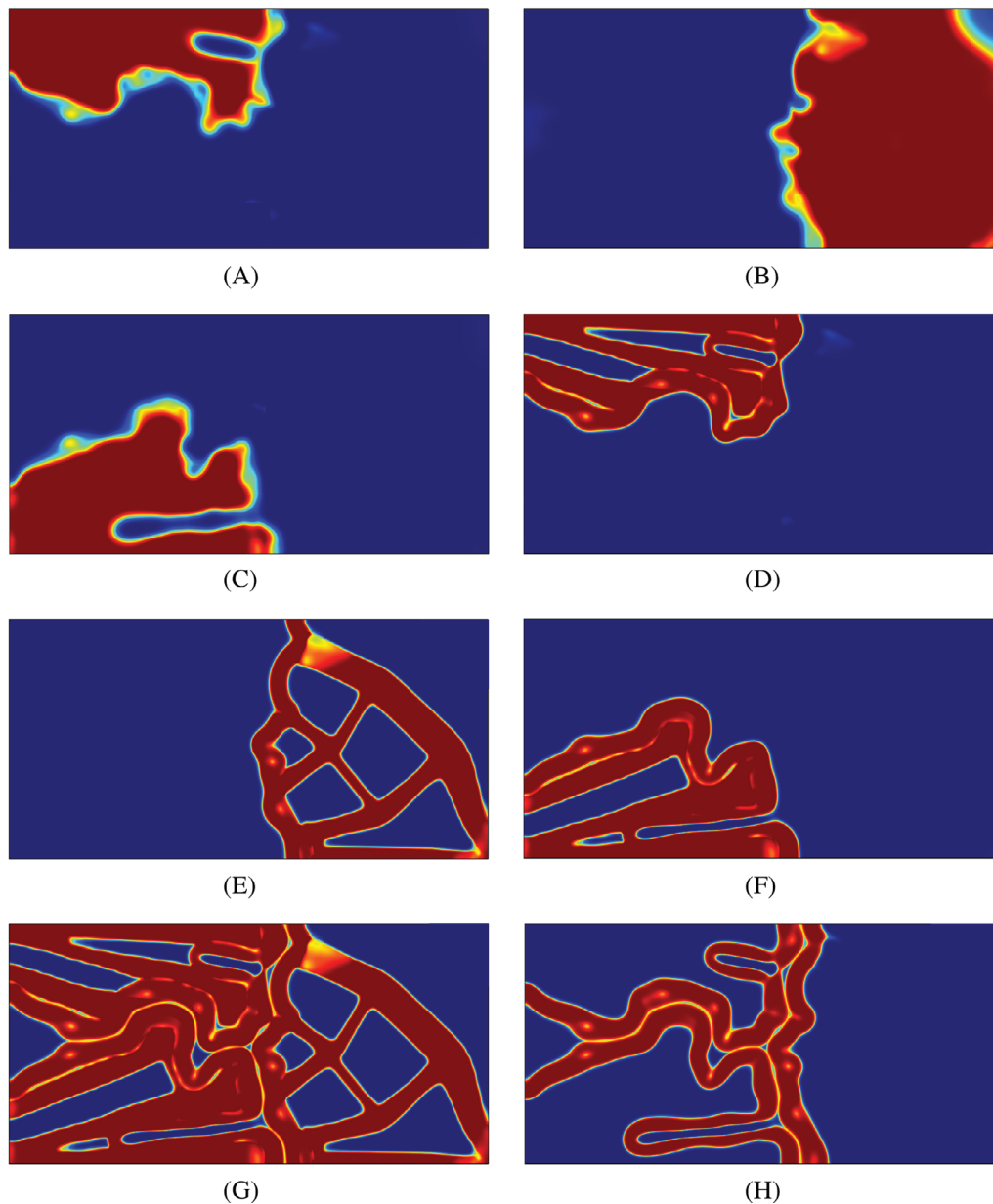
FIGURE 17 Cantilever beam with $K = 3$, $E_{joint} = 0.5$, $r_\mu = 3r_e$, $r_m = 1.75r_e$, $V_{max} = 0.45$, $R_{max} = 0.40$, and $C_{max} = 0.25$: (A) membership 1, (B) membership 2, (C) membership 3, (D) component 1, (E) component 2, (F) component 3, (G) overall structure, and (H) bulk solid boundary and joint. Its optimized structural compliance is 18.030

infill with large structural volume and small interface amount (Figure 29), and the optimizer utilizes more bulk solid boundaries with smaller structural volume and large interface amount (Figure 30). The compliance of these structures are $c = 19.470$ and $c = 20.910$. Owing to large C_{max}, both structures show long and curved component interfaces with many intercomponent gaps. The von Mises stress of these optimized structures are shown in Figure 31. Similar to the earlier results, the stress is much smaller in the regions of bulk-solid boundary and joint, as well as the intercomponent gaps

4.3 | Lightweighting design of a railcar body profile for high-speed trains

This section presents the lightweighting design of a railcar body profile for high-speed trains. The body is manufactured as an assembly of multiple functionally graded lattice components due to the size limitation of the manufacturing
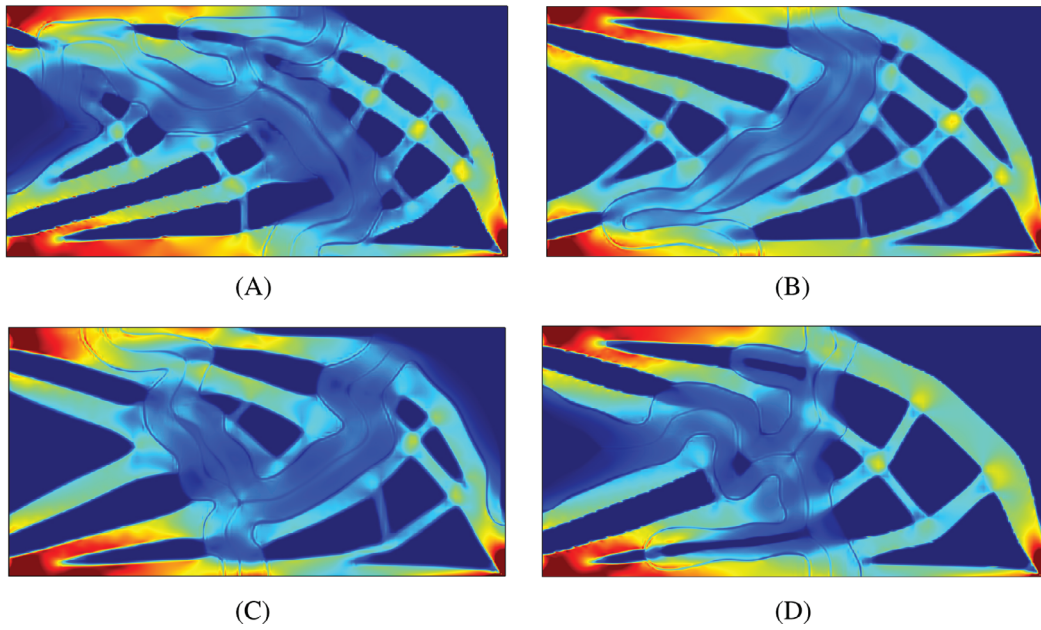
FIGURE 18 Stress of cantilever beam with $K = 3$ and (A) $R_{max} = 0.40$, (B) $R_{max} = 0.55$, (C) $(V_{max}, C_{max}) = (0.5, 0.2)$, and (D) $(V_{max}, C_{max}) = (0.45, 0.25)$
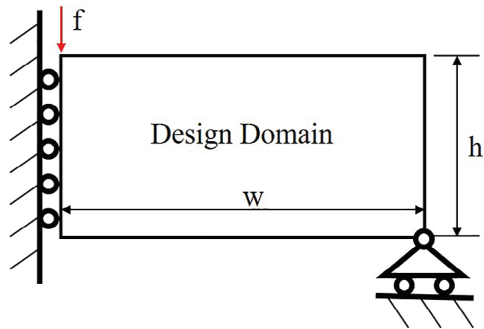

FIGURE 19 Design domain and boundary conditions for the MBB problem
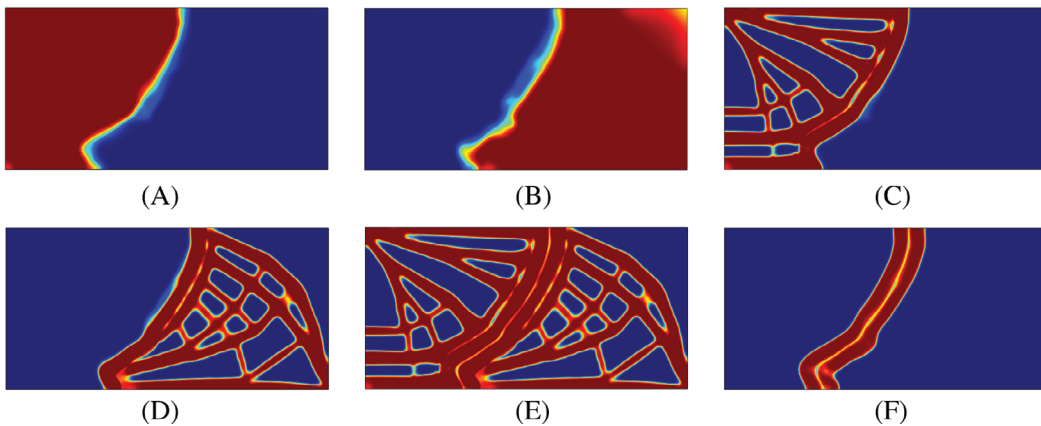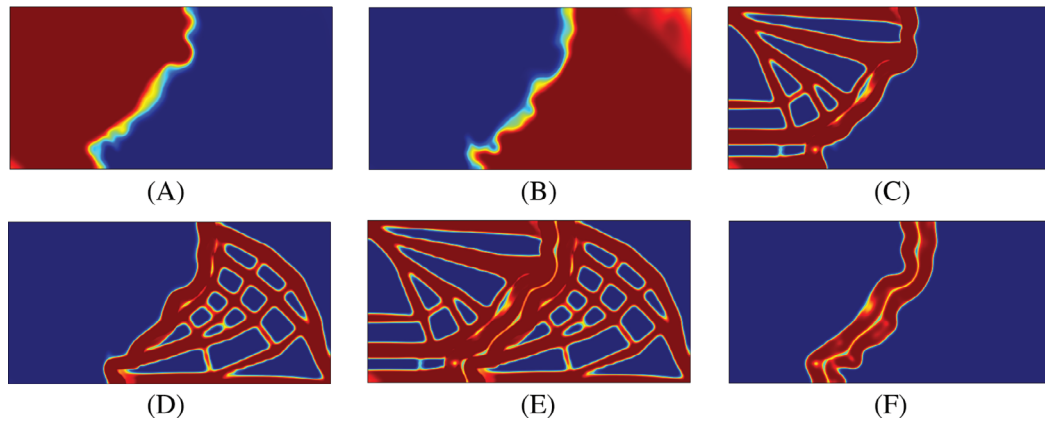

FIGURE 20 MBB with $K = 2$ and $E_{joint} = 0.25$, $r_\mu = 3r_e$, $r_m = 2r_e$, $V_{max} = 0.5$, $R_{max} = 0.55$, and $C_{max} = 0.1$: (A) membership 1, (B) membership 2, (C) component 1, (D) component 2, (E) overall structure, and (F) bulk solid boundary and joint. Its optimized structural compliance is 20.689
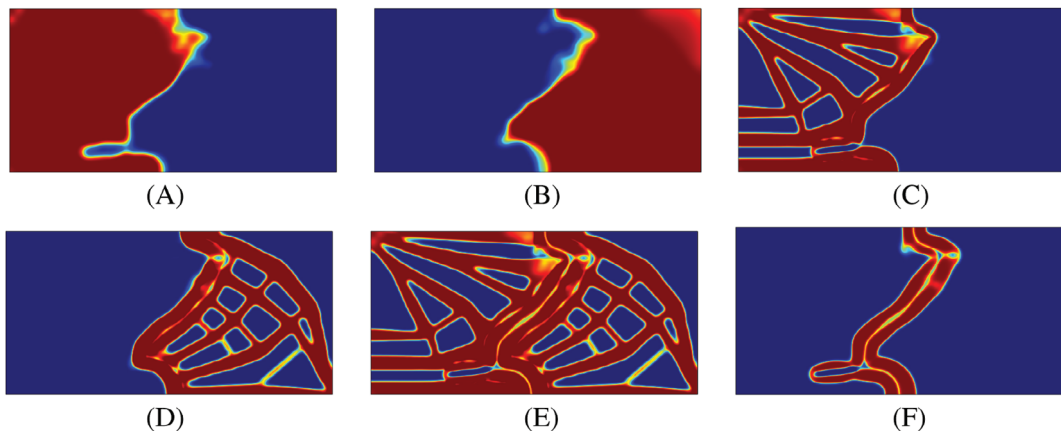
FIGURE 21 MBB with $K = 2$ and $E_{joint} = 0.5$, $r_\mu = 3r_e$, $r_m = 2r_e$, $V_{max} = 0.5$, $R_{max} = 0.55$, and $C_{max} = 0.1$: (A) membership 1, (B) membership 2, (C) component 1, (D) component 2, (E) overall structure, and (F) bulk solid boundary and joint. Its optimized structural compliance is 20.514
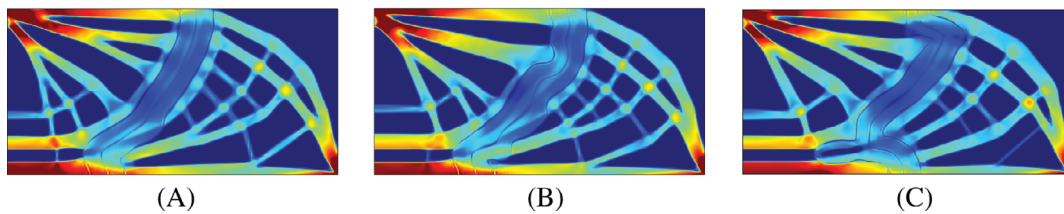

FIGURE 22 MBB with $K = 2$ and $E_{joint} = 0.75$, $r_\mu = 3r_e$, $r_m = 2r_e$, $V_{max} = 0.5$, $R_{max} = 0.55$, and $C_{max} = 0.1$: (A) membership 1, (B) membership 2, (C) component 1, (D) component 2, (E) overall structure, and (F) bulk solid boundary and joint. Its optimized structural compliance is 20.210

FIGURE 23 Stress of MBB with $K = 2$ and (A) $E_{joint} = 0.25$, (B) $E_{joint} = 0.5$, and (C) $E_{joint} = 0.75$

equipment. The design domain shown in Figure 32, where the maximum width $w = 1.8$ and the maximum height $h = 2.9$ with a symmetry constraint on the left edge, and a fixed support on the right bottom, and a distributed load of $p_1 = 1$ is applied in the floor and $p_1 = 0.2$ for the outside surface. In this example, $r_e = 0.01$, the joint stiffness $E_{joint} = 0.5$, $K = 3$, $r_\mu = 8r_e$, $r_m = 4r_e$, $V_{max} = 0.4$, $R_{max} = 0.8$, and $C_{max} = 0.02$ are used. The joint stiffness and cost set to be moderate and small, respectively, which reflects the situation of welded train bodies. Figures 33, shows the optimization results. Similar to the cantilever and MBB examples, the bulk solid boundaries are straight to minimize the length of compliant joints in-between. The von Mises stress in Figure 33(B) shows small stress (shown in blue) in the
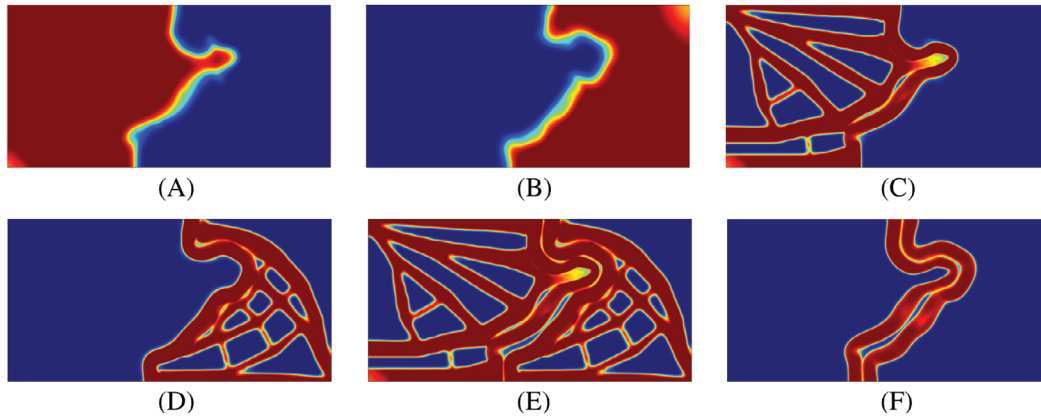
FIGURE 24 MBB with $K = 2$ and $E_{joint} = 0.5$, $r_\mu = 4r_e$, $r_m = 2.25r_e$, $V_{max} = 0.5$, $R_{max} = 0.55$, and $C_{max} = 0.14$: (A) membership 1, (B) membership 2, (C) component 1, (D) component 2, (E) overall structure, and (F) bulk solid boundary and joint. Its optimized structural compliance is 19.703
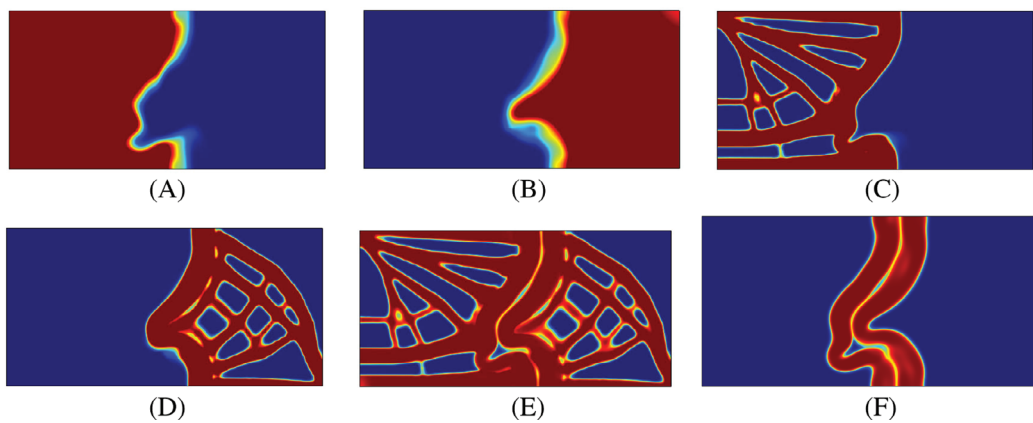

FIGURE 25 MBB with $K = 2$ and $E_{joint} = 0.5$, $r_\mu = 5r_e$, $r_m = 2.75r_e$, $V_{max} = 0.5$, $R_{max} = 0.55$, and $C_{max} = 0.16$: (A) membership 1, (B) membership 2, (C) component 1, (D) component 2, (E) overall structure, and (F) bulk solid boundary and joint. Its optimized structural compliance is 19.108
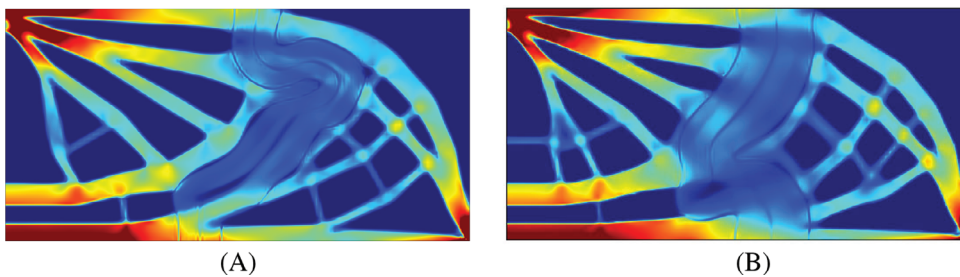

FIGURE 26 Stress of MBB with $K = 2$ and (A) $r_\mu = 4r_e$, $r_m = 2.25r_e$ and (B) $r_\mu = 5r_e$, $r_m = 2.75r_e$
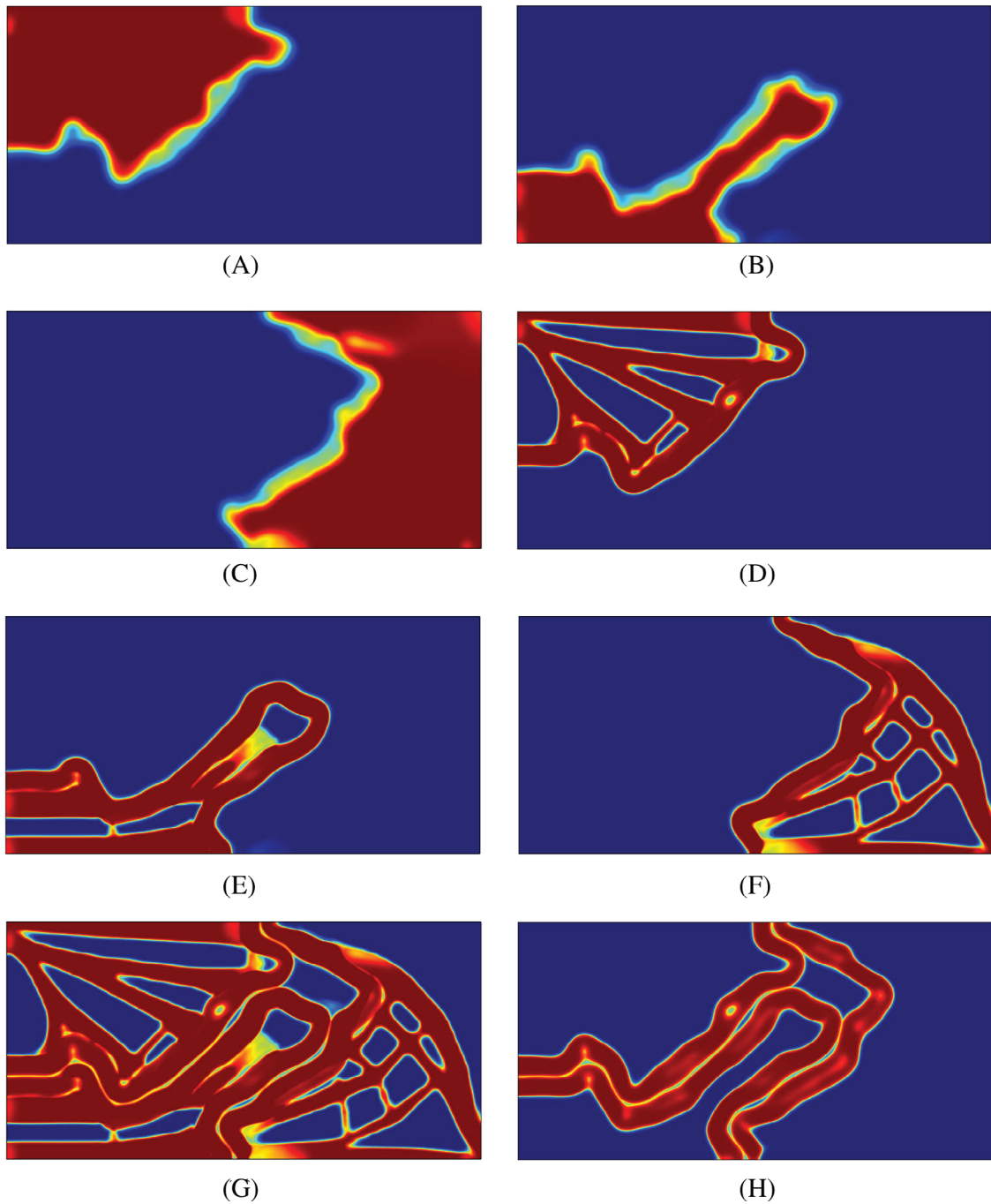
FIGURE 27 MBB with $K = 3$, $E_{joint} = 0.5$, $r_\mu = 4r_e$, $r_m = 2.25r_e$, $V_{max} = 0.5$, $R_{max} = 0.4$, and $C_{max} = 0.18$: (A) membership 1, (B) membership 2, (C) membership 3, (D) component 1, (E) component 2, (F) component 3, (G) overall structure, and (H) bulk solid boundary and joint. Its optimized structural compliance is 20.108

FIGURE 29 MBB with $K = 3$, $E_{joint} = 0.5$, $r_\mu = 3r_e$, $r_m = 1.75r_e$, $V_{max} = 0.5$, $R_{max} = 0.40$, and $C_{max} = 0.25$: (A) membership 1, (B) membership 2, (C) membership 3, (D) component 1, (E) component 2, (F) component 3, (G) overall structure, and (H) bulk solid boundary and joint. Its optimized structural compliance is 19.470
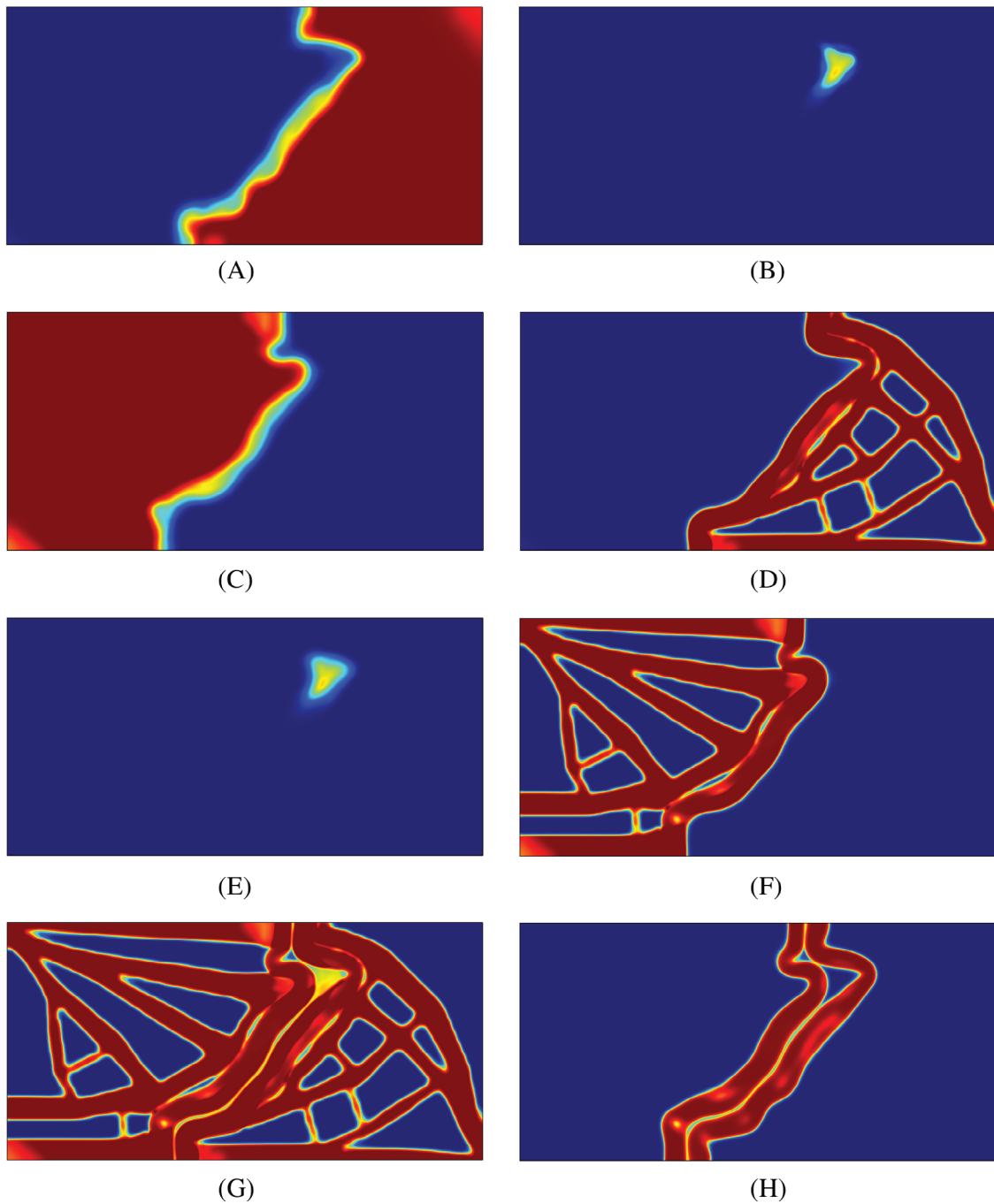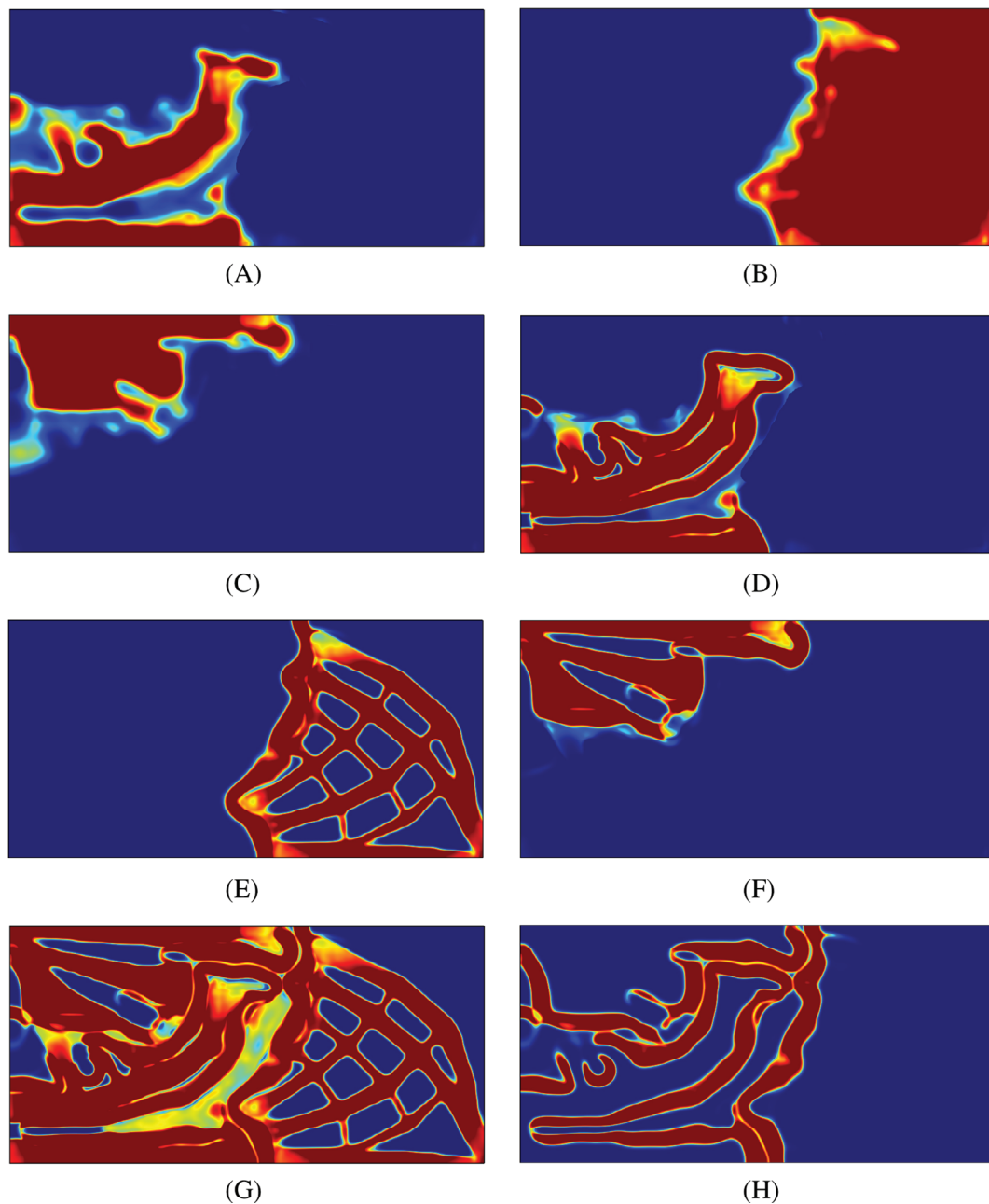
interface regions, which would increase the safety of the structure to reduce the probability of fatigue failure of the joints.

5 | CONCLUSIONS

This article proposed a topology optimization method for structures consisting of multiple lattice components under a certain size, which can be manufactured with an additive manufacturing machine with a size limit. Each component has functionally graded lattice infill surrounded by a bulk solid boundary, which greatly facilitates its assembly via the conventional joining processes such as welding, gluing, riveting, and bolting. The method simultaneously optimizes
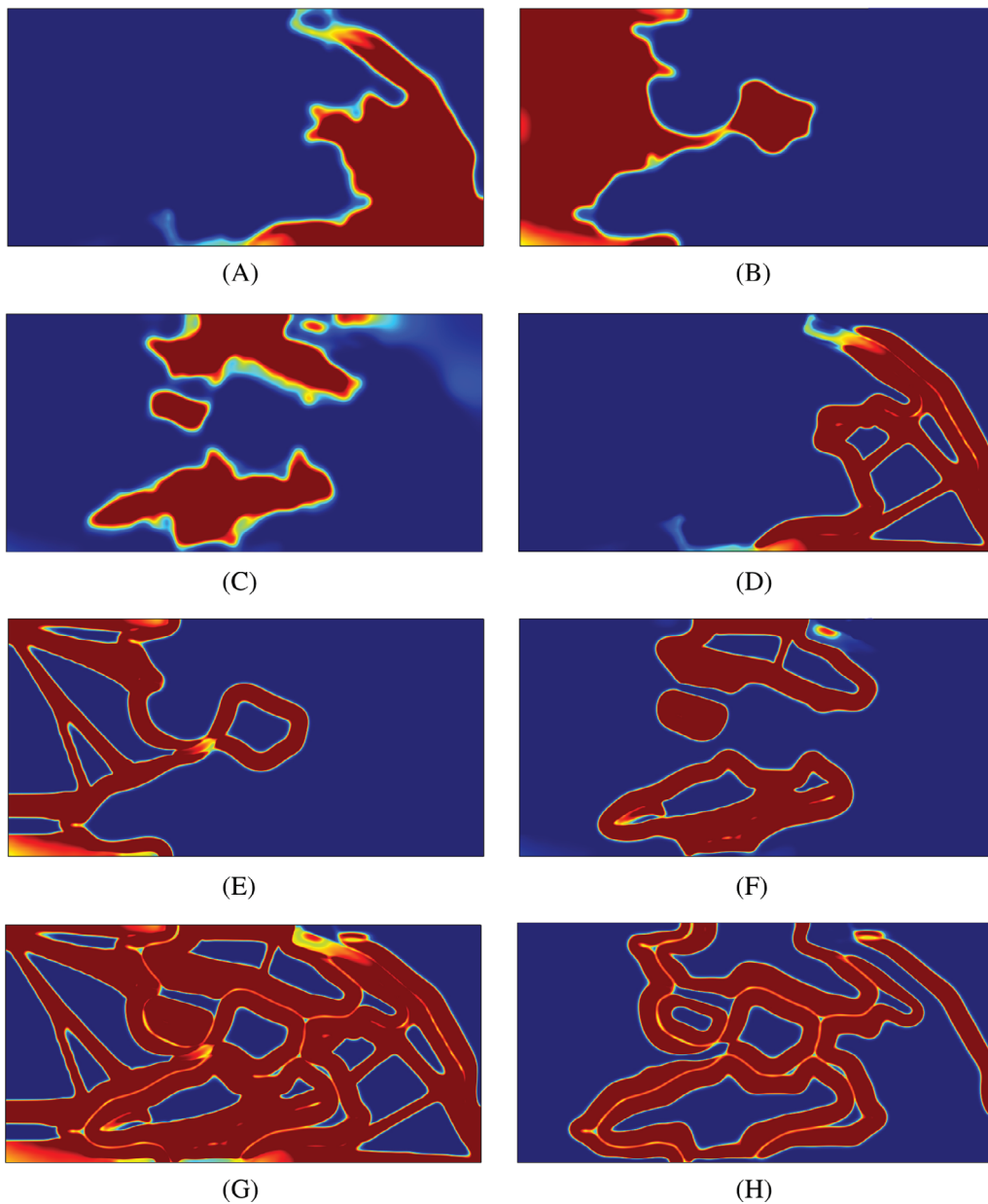
FIGURE 30 MBB with $K = 3$, $E_{joint} = 0.5$, $r_\mu = 3r_e$, $r_m = 1.75r_e$, $V_{max} = 0.4$, $R_{max} = 0.40$, and $C_{max} = 0.35$: (A) membership 1, (B) membership 2, (C) membership 3, (D) component 1, (E) component 2, (F) component 3, (G) overall structure, and (H) bulk solid boundary and joint. Its optimized structural compliance is 20.910

overall structural topology, its partitioning to multiple components, and functionally graded lattice infill within each component. Based on our previous work on the topology optimization of the assemblies of additively manufactured solid components[12] and functionally graded monolithic lattice structures,[13] the novelty of the proposed method beyond these works is threefold: it realizes 1) multiple functionally graded lattice components with guaranteed connectivity of lattices therein, 2) the bulk solid boundaries for each component, which provide continuous mating surfaces between adjacent components, and 3) the structural interfaces between the bulk solid boundaries with a distinct material property, which model the joints (e.g., weld, glue, rivets, and bolts) between the adjacent components. The functionally graded lattice infill with guaranteed connectivity was realized by applying Helmholtz PDE filter with a variable radius, on the density field in the solid isotropic material with penalization (SIMP) method. The partitioning of an overall structure into multiple components was realized by applying the discrete material optimization (DMO) method, in which each material is interpreted as each component. A gradient-free coating filter[38] applied on the component membership field realized

FIGURE 31 Stress of MBB with $K = 3$ and (A) $R_{max} = 0.40$, (B) $R_{max} = 0.55$, (C) $(V_{max}, C_{max}) = (0.5, 0.2)$, and (D) $(V_{max}, C_{max}) = (0.45, 0.25)$
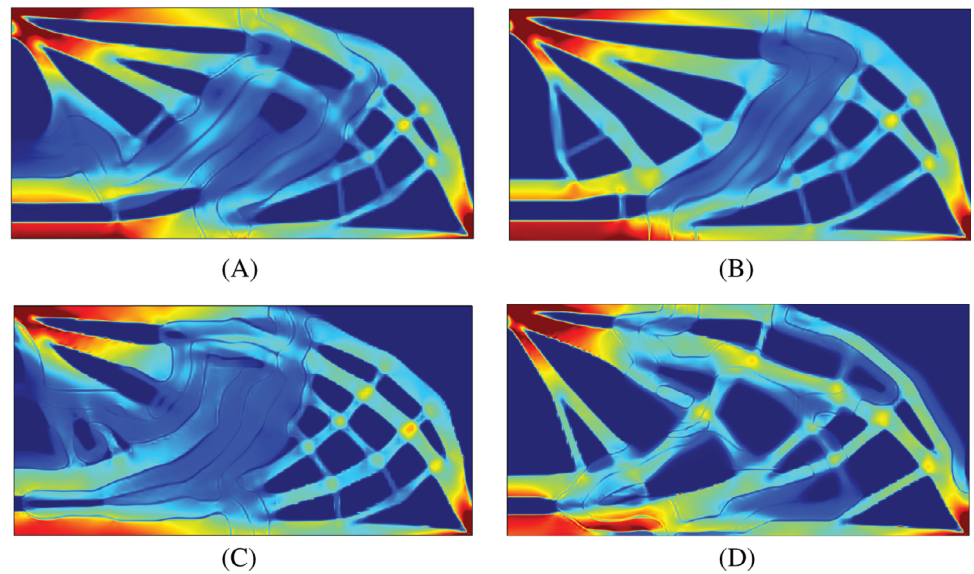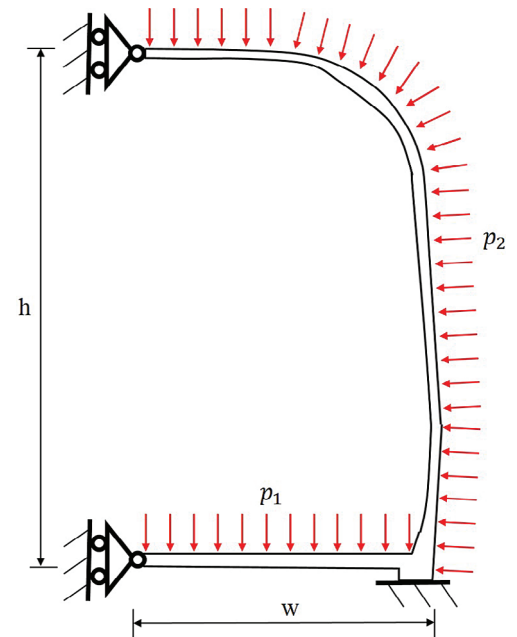

(A)   (B)

(C)   (D)

FIGURE 32 Design domain and boundary conditions for the lightweighting design of a high-speed railcar body profile

the bulk solid boundaries for each component, which provide continuous mating surfaces between adjacent components to enable subsequent joining. The structural interfaces between the bulk solid boundaries were extracted and assigned a distinct material property, which model the joints between the adjacent components. Several numeral examples were solved for demonstration.

The article only presented simple 2D examples, although the proposed formulation is not limited to 2D. Also, joints are idealistically modeled as isotropic, and the constraint models on component size and joint volume are admittedly simple. These simplifications are chosen since, to the best of the authors' knowledge, it is the first time that the manufacturability-driven simultaneous partitioning and topology design for functionally graded lattice structures is presented in the literature. We expect the simple mathematical formulations presented in this article would inform the other researchers to implement more detailed and realistic models, including constraints on maximum stress in joints, guard against buckling in lattices, and tool accessibility to component interfaces for joining.
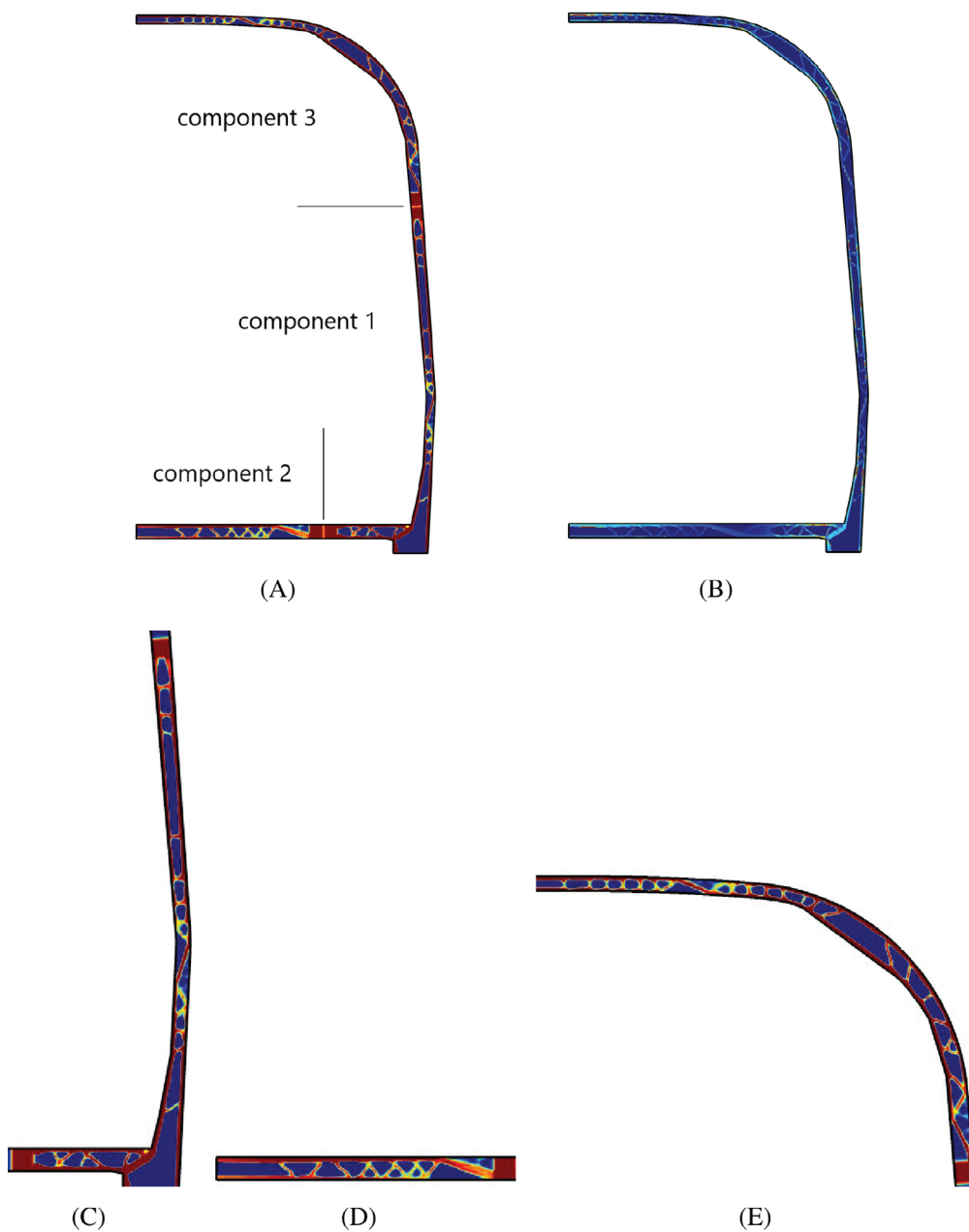
FIGURE 33 Optimized lightweighting design of a high-speed railcar body profile with $K = 3$, $E_{joint} = 0.5$, $r_\mu = 8r_e$, $r_m = 4r_e$, $V_{max} = 0.4$, $R_{max} = 0.8$, and $C_{max} = 0.02$: (A) overall structure, (B) stress, (C) component 1, (D) component 2, and (E) component 3. Its optimized structural compliance is 80.205

DATA AVAILABILITY STATEMENT

Data are available on request from the authors.

ORCID

Bing Yi https://orcid.org/0000-0001-7102-4796

REFERENCES

1. Kadic M, Milton GW, van Hecke M, Wegener M. 3d metamaterials. *Nat Rev Phys.* 2019;1:198-210.

2. Li L, Zhang G, Khandelwal K. Topology optimization of energy absorbing structures with maximum damage constraint. *Int J Numer Methods Eng*. 2017;112:737-775.

3. Jia Z, Wang L. Instability-triggered triply negative mechanical metamaterial. *Phys Rev Appl*. 2019;12:024040.

4. Clausen A, Wang F, Jensen JS, Sigmund O, Lewis JA. Topology optimized architectures with programmable Poisson's ratio over large deformations. *Adv Mater*. 2015;27:5523-5527.

5. Wang Q, Jackson JA, Ge Q, Hopkins JB, Spadaccini CM, Fang NX. Lightweight mechanical metamaterials with tunable negative thermal expansion. *Phys Rev Lett*. 2016;117:175901.

6. L. Wu, B. Li, J. Zhou, Isotropic negative thermal expansion metamaterials, *ACS Appl Mater Interfaces* 8 (2016) 17721–17727. https://doi.org/10.1021/acsami.6b05717, pMID: 27333052.

7. Noguchi Y, Yamada T, Izui K, Nishiwaki S. Topology optimization for hyperbolic acoustic metamaterials using a high-frequency homogenization method. *Comput Methods Appl Mech Eng*. 2018;335:419-471.

8. Cummer SA, Christensen J, Alù A. Controlling sound with acoustic metamaterials. *Nat Rev Mater*. 2016;1:16001.

9. Thompson MK, Moroni G, Vaneker T, et al. Design for additive manufacturing: trends, opportunities, considerations, and constraints. *CIRP Ann*. 2016;65:737-760.

10. Dirrenberger J. From architectured materials to large-scale additive manufacturing. In: Bier H, ed. *Robotic Building*. Springer Series in Adaptive Environments. Berlin, Germany: Springer International Publishing; 2018:79-96.

11. Pham M-S, Liu C, Todd I, Lertthanasarn J. Damage-tolerant architected materials inspired by crystal microstructure. *Nature*. 2019;565:305-311.

12. Zhou Y, Nomura T, Saitou K. Multicomponent topology optimization for additive manufacturing with build volume and cavity free constraints. *J Comput Inf Sci Eng*. 2018;19:021011-021010.

13. Yi B, Zhou Y, Yoon GH, Saitou K. Topology optimization of functionally-graded lattice structures with buckling constraints. *Comput Methods Appl Mech Eng*. 2019;354:593-619.

14. Wu J, Aage N, Westermann R, Sigmund O. Infill optimization for additive manufacturing approaching bone-like porous structures. *IEEE Trans Vis Comput Graph*. 2018;24:1127-1140. https://doi.org/10.1109/TVCG.2017.2655523.

15. Yetis A, Saitou K. Decomposition-based assembly synthesis based on structural considerations. *J Mech Des*. 2002;124:593-601.

16. Lyu N, Saitou K. Decomposition-based assembly synthesis of a three dimensional body-in-white model for structural stiffness. *J Mech Des*. 2003;127:34-48.

17. Lyu N, Saitou K. Decomposition-based assembly synthesis of space frame structures using joint library. *J Mech Des*. 2006;128:57-65.

18. Luo L, Baran I, Rusinkiewicz S, Matusik W. Chopper: partitioning models into 3d-printable parts. *ACM Trans Graph*. 2012;31:129:1-129:9.

19. Yao M, Chen Z, Luo L, Wang R, Wang H. Level-set-based partitioning and packing optimization of a printable model. *ACM Trans Graph*. 2015;34:214:1-214:11.

20. Liu H-Y, Fu X-M, Ye C, Chai S, Liu L. Atlas refinement with bounded packing efficiency. *ACM Trans Graph*. 2019;38:33:1-33:13.

21. Johanson R, Kikuchi N, Papalambros P, Topping B, Papadrakakis M. Simultaneous topology and material microstructure design. *Conference on computational structures technology*. 1994.

22. Jiang T, Chirehdast M. A systems approach to structural topology optimization: designing optimal connections. *ASME J Mech Des*. 1997:119(1):40-47. https://doi.org/10.1115/1.2828787.

23. Chickermane H, Gea HC. Design of multi-component structural systems for optimal layout topology and joint locations. Engineering with Computers 13. 1996:235-243. https://doi.org/10.1007/BF01200050.

24. Li Q, Steven GP, Xie YM. Evolutionary structural optimization for connection topology design of multi-component systems. *Eng Comput*. 2001;18(3/4):460-479.

25. Pollini N, Amir O. Mixed projection-and density-based topology optimization with applications to structural assemblies. *Struct Multidiscip Optim*. 2020;61:687-710.

26. Lyu N, Saitou K. Topology optimization of multicomponent beam structure via decomposition-based assembly synthesis. *ASME J Mech Des*. 2005;127(2):170-183. https://doi.org/10.1115/1.1814671.

27. Yildiz AR, Saitou K. Topology synthesis of multicomponent structural assemblies in continuum domains. *J Mech Des*. 2011;133(1):011008.

28. Guirguis D, Hamza K, Aly M, Hegazi H, Saitou K. Multi-objective topology optimization of multi-component continuum structures via a kriging-interpolated level set approach. *Struct Multidiscip Optim*. 2015;51:733-748.

29. Zhou Y, Saitou K. Gradient-based multi-component topology optimization for stamped sheet metal assemblies(mto-s). *Struct Multidiscip Optim*. 2018;58:83-94.

30. Zhou Y, Nomura T, Saitou K. Multi-component topology and material orientation design of composite structures (mto-s). *Comput Methods Appl Mech Eng*. 2018;342:438-457.

31. Campagna F, Diaz AR. Optimization of lattice infill distribution in additive manufacturing. Paper presented at: Proceedings of the International Design Engineering Technical Conferences and Computers and Information in Engineering Conference; 2017; ASME, Cleveland, Ohio.

32. Gao J, Luo Z, Li H, Gao L. Topology optimization for multiscale design of porous composites with multi-domain microstructures. *Comput Methods Appl Mech Eng*. 2019;344:451-476.

33. Vermaak N, Michailidis G, Parry G, Estevez R, Allaire G, Bréchet Y. Material interface effects on the topology optimizationof multi-phase structures using a level set method. *Struct Multidiscip Optim*. 2014;50:623-644.

34. Faure A, Michailidis G, Parry G, Vermaak N, Estevez R. Design of thermoelastic multi-material structures with graded interfaces using topology optimization. *Struct Multidiscip Optim*. 2017;56:823-837.

35. Liu P, Kang Z. Integrated topology optimization of multi-component structures considering connecting interface behavior. *Comput Methods Appl Mech Eng*. 2018;341:851-887.

36. Chu S, Xiao M, Gao L, Li H, Zhang J, Zhang X. Topology optimization of multi-material structures with graded interfaces. *Comput Methods Appl Mech Eng*. 2019;346:1096-1117.

37. Clausen A, Aage N, Sigmund O. Topology optimization of coated structures and material interface problems. *Comput Methods Appl Mech Eng*. 2015;290:524-541.

38. Yoon GH, Yi B. A new coating filter of coated structure for topology optimization. *Struct Multidiscip Optim*. 2019;60;1527-1544. https://doi.org/10.1007/s00158-019-02279-7.

39. Lazarov BS, Sigmund O. Filters in topology optimization based on helmholtz-type differential equations. *Int J Numer Methods Eng*. 2011;86:765-781.

40. Stegmann J, Lund E. Discrete material optimization of general composite shell structures. *Int J Numer Methods Eng*. 2005;62:2009-2027.

41. Svanberg K. The method of moving asymptotes – a new method for structural optimization. *Int J Numer Methods Eng*. 1987;24:359-373.

APPENDIX A. SENSITIVITIES

This appendix presents the sensitivities of the objective function and constraints in Equation (18) with respect to design variables ϕ, μ, and r_l. The partial derivatives of intermediate variables ρ, ρ_l, $m^{(k)}$, and $b^{(k)}$, which these sensitivities depend on, are also presented in Section A.5.

A.1 Sensitivity of the objective

Using the adjoint method, the sensitivity of the objective function $f := \mathbf{U}^{\mathrm{T}} \mathbf{K} \mathbf{U}$ subject to the static equilibrium $\mathbf{K} \mathbf{U} = \mathbf{F}$ is derived as:

$$\frac{\mathrm{d}f}{\mathrm{d}\phi} = -\mathbf{U}^{\mathrm{T}} \frac{\partial \mathbf{K}}{\partial \phi} \mathbf{U} = -\mathbf{U}^{\mathrm{T}} \mathbf{K}^0 \mathbf{U} \frac{\partial E_t}{\partial \phi}, \tag{A1}$$

$$\frac{\mathrm{d}f}{\mathrm{d}\mu^{(k)}} = -\mathbf{U}^{\mathrm{T}} \frac{\partial \mathbf{K}}{\partial \mu^{(k)}} \mathbf{U} = -\mathbf{U}^{\mathrm{T}} \mathbf{K}^0 \mathbf{U} \frac{\partial E_t}{\partial \mu^{(k)}}, \tag{A2}$$

$$\frac{\mathrm{d}f}{\mathrm{d}r_l} = -\mathbf{U}^{\mathrm{T}} \frac{\partial \mathbf{K}}{\partial r_l} \mathbf{U} = -\mathbf{U}^{\mathrm{T}} \mathbf{K}^0 \mathbf{U} \frac{\partial E_t}{\partial r_l}, \tag{A3}$$

where $\mathbf{K} = E_t \mathbf{K}^0$. Using Equation (17), the partial derivatives of E_t can be given as:

$$\frac{\partial E_t}{\partial \phi} = E \sum_{k=1}^{K} \left\{ p_\rho \rho^{\,p_\rho - 1} \frac{\partial \rho}{\partial \phi} m^{(k)} + g'(\rho_l) \frac{\partial \rho_l}{\partial \phi} b^{(k)} - 2g'(\rho_l) \frac{\partial \rho_l}{\partial \phi} \sum_{l=1}^{k} J^{(kl)} \right\}, \tag{A4}$$

$$\frac{\partial E_t}{\partial \mu^{(k)}} = E \left[\rho^{p_\rho} \frac{\partial m^{(k)}}{\partial \mu^{(k)}} - \{1 - g(\rho_l)\} \frac{\partial b^{(k)}}{\partial \mu^{(k)}} \right.$$
$$\left. - \{1 + 2g(\rho_l) - \eta\} (1 - m_0) \frac{\partial b^{(k)}}{\partial \mu^{(k)}} \left\{ m_0 + b^{(l)}(1 - m_0) \right\} \right] \tag{A5}$$

$$\frac{\partial E_t}{\partial r_l} = E \sum_{k=1}^{K} \left\{ g'(\rho_l) \frac{\partial \rho_l}{\partial r_l} b^{(k)} - 2g'(\rho_l) \frac{\partial \rho_l}{\partial r_l} \sum_{l=1}^{k} J^{(kl)} \right\}. \tag{A6}$$

A.2 Sensitivity of global and local volume constraint

The sensitivity of the constraint function on the entire structural volume $g_1 := \int_D \sum_{k=1}^{K} \rho m^{(k)} dx - V_{max}$ is given:

$$\frac{\partial g_1}{\partial \phi} = \int_D \sum_{k=1}^{K} \frac{\partial \rho}{\partial \phi} m^{(k)} dx, \tag{A7}$$

$$\frac{\partial g_1}{\partial \mu^{(k)}} = \int_D \sum_{k=1}^{K} \rho \frac{\partial m^{(k)}}{\partial \mu^{(k)}} dx, \tag{A8}$$

$$\frac{\partial g_1}{\partial r_l} = 0. \tag{A9}$$

Similarly, the sensitivity of the constraint function on the locally averaged density $g_2 := \left(\int_D \rho_l^p dx \right)^{\frac{1}{p}} - P_{max}$ is given as:

$$\frac{\partial g_2}{\partial \phi} = \left(\int_D \rho_l^p dx \right)^{\frac{1}{p}-1} \int_D \rho_l^{p-1} \frac{\partial \rho_l}{\partial \phi} dx, \tag{A10}$$

$$\frac{\partial g_2}{\partial \mu^{(k)}} = 0, \tag{A11}$$

$$\frac{\partial g_2}{\partial r_l} = \left(\int_D \rho_l^p dx \right)^{\frac{1}{p}-1} \int_D \rho_l^{p-1} \frac{\partial \rho_l}{\partial r_l} dx. \tag{A12}$$

A.3 Sensitivity of bounding sphere

The sensitivity of the constraint function on the bounding sphere $g_3 := R^{(k)} - R_{max}$ is given as:

$$\frac{\partial g_3}{\partial \phi} = \frac{1}{p} \left[\int_D \rho m^{(k)} \left\{ x - x_c^{(k)} \right\}^p dx \right]^{\frac{1}{p}-1}$$
$$\times \int_D \left[\frac{\partial \rho}{\partial \phi} m^{(k)} \left\{ x - x_c^{(k)} \right\}^p - p\rho m^{(k)} \left\{ x - x_c^{(k)} \right\}^{p-1} \frac{\partial x_c^{(k)}}{\partial \phi} \right] dx, \tag{A13}$$

$$\frac{\partial g_3}{\partial \mu^{(k)}} = \frac{1}{p} \left[\int_D \rho m^{(k)} \left\{ x - x_c^{(k)} \right\}^p dx \right]^{\frac{1}{p}-1}$$
$$\times \int_D \left[\rho \frac{\partial m^{(k)}}{\partial \mu^{(k)}} \left\{ x - x_c^{(k)} \right\}^p - p\rho m^{(k)} \left\{ x - x_c^{(k)} \right\}^{p-1} \frac{\partial x_c^{(k)}}{\partial \mu^{(k)}} \right] dx, \tag{A14}$$

$$\frac{\partial g_3}{\partial r_l} = 0, \tag{A15}$$

where

$$\frac{\partial x_c^{(k)}}{\partial \phi} = \frac{\int_D \frac{\partial \rho}{\partial \phi} m^{(k)} x dx \times \int_D \rho m^{(k)} dx - \int_D \rho m^{(k)} x dx \times \int_D \frac{\partial \rho}{\partial \phi} m^{(k)} dx}{\left\{ \int_D \rho m^{(k)} dx \right\}^2}, \tag{A16}$$

$$\frac{\partial x_c^{(k)}}{\partial \mu^{(k)}} = \frac{\int_D \rho \frac{\partial m^{(k)}}{\partial \mu^{(k)}} x dx \times \int_D \rho m^{(k)} dx - \int_D \rho m^{(k)} x dx \times \int_D \rho \frac{\partial m^{(k)}}{\partial \mu^{(k)}} dx}{\left\{ \int_D \rho m^{(k)} dx \right\}^2}. \tag{A17}$$

A.4 Sensitivity of joint cost constraint

The sensitivity of the constraint function on the bulk solid boundaries and joints $g_4 := C - C_{max}$ is given as:

$$\frac{\partial g_4}{\partial \phi} = \sum_{k=1}^{K} \left[\int_D g'(\rho_l) \frac{\partial \rho_l}{\partial \phi} \left\{ m^{(k)} - \sum_{l=1}^{k} J^{(kl)} \right\} dx \right], \tag{A18}$$

$$\frac{\partial g_4}{\partial \mu^{(k)}} = \sum_{k=1}^{K} \left[\int_D g(\rho_l) \left[\frac{\partial m^{(k)}}{\partial \mu^{(k)}} - \frac{\partial b^{(k)}}{\partial \mu^{(k)}} (1 - m_0) \left\{ m_0 - b^{(l)} (1 - m_0) \right\} \right] dx \right], \tag{A19}$$

$$\frac{\partial g_4}{\partial r_l} = \sum_{k=1}^{K} \left[\int_D g'(\rho_l) \frac{\partial \rho_l}{\partial r_l} \left\{ m^{(k)} - \sum_{l=1}^{k} J^{(kl)} \right\} dx \right]. \tag{A20}$$

A.5 Sensitivity of intermediate variables

The partial derivatives of ρ and ρ_l with respect to ϕ are given by Equations (1), (2), and (3) as:

$$\frac{\partial \rho_l}{\partial \phi} = \frac{\partial \rho_l}{\partial \rho} \frac{\partial \rho}{\partial \phi}, \tag{A21}$$

$$\frac{\partial \rho_l}{\partial \rho} = \left(\mathop{A}_{e=1}^{n_e} \mathbf{N}_e^{\mathrm{T}} \right)^{\mathrm{T}} \left[\mathbf{K}_f^{-1}(r_l) \mathop{A}_{e=1}^{n_e} \left(\int_{D_e} \mathbf{N}_e^{\mathrm{T}} dx \right) \right], \tag{A22}$$

$$\frac{\partial \rho}{\partial \phi} = \frac{\partial \rho}{\partial \overline{\phi}} \frac{\partial \overline{\phi}}{\partial \phi}, \tag{A23}$$

$$\frac{\partial \rho}{\partial \overline{\phi}} = \frac{\partial H_s(\overline{\phi})}{\partial \overline{\phi}} = \delta(\overline{\phi}), \tag{A24}$$

$$\frac{\partial \overline{\phi}}{\partial \phi} = \left(\mathop{A}_{e=1}^{n_e} \mathbf{N}_e^{\mathrm{T}} \right)^{\mathrm{T}} \left[\mathbf{K}_f^{-1}(r_\rho) \mathop{A}_{e=1}^{n_e} \left(\int_{D_e} \mathbf{N}_e^{\mathrm{T}} dx \right) \right], \tag{A25}$$

where A is the standard finite element assembly operator, n_e is the number of elements, $\mathbf{N}_e$ and D_e are the vector of the element shape functions and the domain of finite element e, respectively, for solving the Helmholtz filter functions, and

$$\mathbf{K}_f(r) = \mathop{A}_{e=1}^{n_e} \left[\int_{D_e} \left\{ -(\nabla \mathbf{N}_e)^{\mathrm{T}} r^2 \nabla \mathbf{N}_e + \mathbf{N}_e^{\mathrm{T}} \mathbf{N}_e \right\} dx \right]. \tag{A26}$$

The details of the derivation is described in Reference 39. Since both ρ and ρ_l do not depends on $\mu^{(k)}$:

$$\frac{\partial \rho_l}{\partial \mu^{(k)}} = \frac{\partial \rho}{\partial \mu^{(k)}} = 0. \tag{A27}$$

Similarly, ρ does not depend on r_l, hence:

$$\frac{\partial \rho}{\partial r_l} = 0. \tag{A28}$$

From Equation (3), $\partial \rho_l / \partial r_l$ is given as:

$$\frac{\partial \rho_l}{\partial r_l} = \left(\mathop{A}_{e=1}^{n_e} \mathbf{N}_e^{\mathrm{T}} \right)^{\mathrm{T}} \left[\mathbf{K}_f^{-1}(r_l) \mathop{A}_{e=1}^{n_e} \left(\int_{D_e} (\nabla \mathbf{N}_e)^{\mathrm{T}} 2r_l \nabla \mathbf{N}_e dx \right) \right]. \tag{A29}$$

Since $m^{(k)}$ and $b^{(k)}$ do not depend on either ϕ or r_l:

$$\frac{\partial m^{(k)}}{\partial \phi} = \frac{\partial m^{(k)}}{\partial r_l} = \frac{\partial b^{(k)}}{\partial \phi} = \frac{\partial b^{(k)}}{\partial r_l} = 0. \tag{A30}$$

The partial derivatives of $m^{(k)}$ and $b^{(k)}$ with respect to $\mu^{(k)}$ are given by Equations (9), (10), (11), (7), and (8) as:

$$\frac{\partial b^{(k)}}{\partial \mu^{(k)}} = -\omega^{(k)} \frac{\partial m^{(k)}}{\partial \mu^{(k)}} + (1 - m^{(k)}) \frac{\partial \omega^{(k)}}{\partial \mu^{(k)}}, \tag{A31}$$

where

$$\frac{\partial \omega^{(k)}}{\partial \mu^{(k)}} = \frac{\partial \omega^{(k)}}{\partial \overline{m}^{(k)}} \frac{\partial \overline{m}^{(k)}}{\partial m^{(k)}} \frac{\partial m^{(k)}}{\partial \mu^{(k)}}, \tag{A32}$$

$$\frac{\partial \omega^{(k)}}{\partial \overline{m}^{(k)}} = \frac{\partial H_r(\overline{m}^{(k)})}{\partial \overline{m}^{(k)}} = \delta(\overline{m}^{(k)}), \tag{A33}$$

$$\frac{\partial \overline{m}^{(k)}}{\partial m^{(k)}} = \left(\underset{e=1}{\overset{n_e}{A}} \mathbf{N}_e^{\mathrm{T}} \right)^{\mathrm{T}} \left[\mathbf{K}_f^{-1}(r_m) \underset{e=1}{\overset{n_e}{A}} \left(\int_{D_e} \mathbf{N}_e^{\mathrm{T}} dx \right) \right], \tag{A34}$$

$$\frac{\partial m^{(k)}}{\partial \mu^{(k)}} = P_m \left\{ \overline{\mu}^{(k)} \right\}^{P_m - 1} \frac{\partial \overline{\mu}^{(k)}}{\partial \mu^{(k)}} \prod_{i=1, i \neq k}^{K} \left[1 - \left\{ \overline{\mu}^{(i)} \right\}^{P_m} \right], \tag{A35}$$

$$\frac{\partial \overline{\mu}^{(k)}}{\partial \mu^{(k)}} = \left(\underset{e=1}{\overset{n_e}{A}} \mathbf{N}_e^{\mathrm{T}} \right)^{\mathrm{T}} \left[\mathbf{K}_f^{-1}(r_\mu) \underset{e=1}{\overset{n_e}{A}} \left(\int_{D_e} \mathbf{N}_e^{\mathrm{T}} dx \right) \right]. \tag{A36}$$